arXiv:1206.4475v1 [q-bio.BM] 20 Jun 2012

Non-specific binding of Na^+ and Mg^{2+} to RNA determined by force spectroscopy methods

C. V. Bizarro[a,b,†,**], A. Alemany[a,b,**], F. Ritort[a,b,*]

[a]Departament de Física Fonamental, Universitat de Barcelona, Diagonal 647, 08028 Barcelona, Spain; [b]CIBER-BBN de Bioingeniería, Biomateriales y Nanomedicina, Instituto de Sanidad Carlos III, Madrid, Spain; †Present Address: Centro de Pesquisas em Biologia Molecular e Funcional/PUCRS Avenida Ipiranga 6681, Tecnopuc, Partenon 90619-900, Porto Alegre, RS, Brazil

*To whom correspondence should be addressed. Tel: +34-934035869; Fax: +34-934021149; Email: fritort@gmail.com, ritort@ffn.ub.es

**These authors contributed equally to the paper

Abstract

RNA duplex stability depends strongly on ionic conditions, and inside cells RNAs are exposed to both monovalent and multivalent ions. Despite recent advances, we do not have general methods to quantitatively account for the effects of monovalent and multivalent ions on RNA stability, and the thermodynamic parameters for secondary structure prediction have only been derived at 1M [Na^+]. Here, by mechanically unfolding and folding a 20 bp RNA hairpin using optical tweezers, we study the RNA thermodynamics and kinetics at different monovalent and mixed monovalent/Mg^{2+} salt conditions. We measure the unfolding and folding rupture forces and apply Kramers theory to extract accurate information about the hairpin free energy landscape under tension at a wide range of ionic conditions. We obtain non-specific corrections for the free energy of formation of the RNA hairpin and measure how the distance of the transition state to the folded state changes with force and ionic strength. We experimentally validate the Tightly Bound Ion model and obtain values for the persistence length of ssRNA. Finally, we test the approximate rule by which the non-specific binding affinity of divalent cations at a given concentration is equivalent to that of monovalent cations taken at 100 fold that concentration for small molecular constructs.

1 Introduction

RNA hairpins are elementary structures found in many macromolecular assemblies. It is generally accepted that a deeper understanding of their dynamics is a critical step towards the elucidation of many biological processes, like the regulation of gene expression [1, 2, 3, 4, 5]; the catalytic activity in many reactions [6, 7]; the ligand-binding specificity [8]; or the RNA folding problem [9, 10]. DNA and RNA hairpins are also appealing model systems for their simplicity as they are amenable to exhaustive studies using a more physically-oriented approach, where theoretical models can be rigorously tested using simulations and experiments [11, 12].

Many different and complementary biophysical methods have been used to study these structures. For example, using time-resolved nuclear magnetic resonance (NMR) spectroscopy and thermal denaturation experiments, kinetics and thermodynamics of bistable RNA molecules were studied [13, 14, 15, 16, 17, 18, 19, 20, 21, 22]. Recently, a photolabile caged RNA was designed to stabilize one ground-state conformation and study the folding kinetics by NMR and CD spectroscopy under different conditions, including Mg^{2+} [23]. Laser temperature-jump experiments have also been used to characterize the folding kinetics of small RNA hairpins at the ns and μs timescales [24, 25, 26, 27, 28, 29]. Using coarse-grained Go-like models, it was predicted that hairpins unfold in an all-or-none process in mechanical experiments [30], in agreement with experimental results [31, 32, 33].

Within the cell, many dynamical processes involving transient melting events of DNA and RNA double strands are driven by the application of localized forces by molecular motors. Therefore, single-molecule experiments are ideal to understand the thermodynamics and kinetics of macromolecules inside cells [34, 35]. As pointed out by Hyeon *et al.* [30], force-denaturation using single-molecule experiments are intrinsically different from thermally-induced denaturation: in bulk experiments where the unfolded state is accessed by raising the temperature or lowering the concentration of ions, the unfolded state is a high-entropy state while in mechanical pulling experiments the unfolding process is a transition from a low-entropy state to another low-entropy state. Regions of the free energy landscape normally inaccessible by conventional methods are probed using mechanical experiments. Consequently, pathways and rates of thermally-induced and mechanical unfolding processes are expected to be different.

In a previous work [36] we pulled an RNA hairpin using optical tweezers [37, 38] to study the base-pairing thermodynamics, kinetics and mechanical properties at a fixed monovalent condition. A kinetic analysis was introduced to determine the location of the force-dependent kinetic barrier, the attempt rate, and the free energy of formation of the molecule. Here we performed a systematic study by mechanically pulling the same RNA hairpin at different monovalent cation concentrations and also at mixed ionic conditions containing different concentrations of Mg^{2+} cations. This is important because RNAs are highly charged polyanions whose stability strongly depends on solvent ionic conditions [39, 40, 41, 42, 43]. Despite its biological significance, we have limited information about RNA helix stability in mixed monovalent/multivalent ionic conditions [44, 45]. In fact, the thermodynamic parameters for secondary structural elements of RNAs have

only been derived at the fixed standard salt condition of 1M [Na^+] [15, 16, 17, 18, 19, 20, 21]. Here we derived numbers such as the persistence length describing the elastic response of ssRNA and also the free energy of formation of an RNA hairpin at different monovalent and mixed monovalent/Mg^{2+} conditions. Our results are compatible with predictions obtained using the Tightly Bound Ion (TBI) model for mixed ion solutions, that treats monovalent ions as ionic background and multivalent ions as responsible from ion-ion correlation effects, and which takes into account only non-sequence-specific electrostatic effects of ions on RNA [43, 44, 45]. Our findings demonstrate the validity of the approximate rule by which the non-specific binding affinity of divalent cations is equal to that of monovalent cations taken around 100 fold concentration for small molecular constructs [46, 47].

2 Materials and Methods

2.1 Molecular Synthesis

The RNA molecule was prepared as previously described [48]. Oligonucleotides CD4F (5'-AATTCACACG CGAGCCATAA TCTCATCTGG AAACAGATGAG ATTA TGGCTCGC ACACA-3') and CD4R (5'-AGCTTGTGT GCGAGCCATA ATCTCATC TGTTTCCAGAT GAGAT-TATGGC TCGCGTGTG-3') were annealed and cloned into the pBR322 DNA plasmid (GenBank J01749) digested with EcoRI (position 4360) and HindIII (position 30). The annealed oligonucleotides contain the sequence that codes for a modified version of CD4-42F class I hairpin that targets the mRNA of the CD4 receptor of the human immunodeficiency virus [49]. Oligonucleotides T7_Forward (5'-TAATACGACTCA CTATAGG GACTGGTGA GTACTCA ACCAAGTC-3') and T7_Reverse (5'-TA GGAAGC AGCCCAGT AGTAGG-3') were used as primers to amplify by PCR a product of 1201 bp from the recombinant clone containing the CD4 insert. This amplicon contains the T7 RNA Polymerase promoter at one end, and was used as a template to synthesize an RNA containing the RNA hairpin (20bp stem sequence and tetraloop GAAA) and the RNA components of handles A (527 bp) and B (599 bp). The DNA components of handles A and B were obtained by PCR from the pBR322 vector (positions 3836-1 for handle A and positions 31-629 for handle B). Handle A was 3' biotinylated while handle B was tagged with a 5' digoxigenin. Hybridization reactions were performed in a formamide-based buffer [50] with a step-cool temperature program: denaturation at 85°C for 10 min, followed by 1.5 h incubation at 62°C, 1.5 h incubation at 52 °C, and finished with a cooling to 10°C within 10 min.

2.2 Measurement Protocol

All experiments were performed using a dual-beam force measuring optical trap [37, 38] at 25±1 °C in buffers containing 100 mM Tris.HCl (pH 8.1), 1mM EDTA, and NaCl concentrations of 0, 100, 500, and 1000 mM, or in buffers containing 100 mM Tris.HCl (pH 8.1) and $MgCl_2$

concentrations of 0.01, 0.1, 0.5, 1, 4, and 10 mM. The monovalent cation concentration [Mon^+] includes the contributions from [Na^+] ions and dissociated [$Tris^+$] ions. At 25°C and pH 8.1, about half of the Tris molecules are protonated, therefore 100 mM Tris buffer adds 50 mM to the total monovalent ion concentration [51]. Anti-digoxigenin polyclonal antibody-coated polystyrene microspheres (AD beads) of 3.0-3.4 μm (Spherotech, Libertyville, IL) were incubated at room temperature with the molecular construct for 20 min. The second attachment was achieved inside the microfluidics chamber using a single optically trapped AD bead previously incubated with the RNA hairpin and a streptavidin-coated polystyrene microsphere (SA bead) of 2.0-2.9 μm (G. Kisker GbR, Products for Biotechnologie) positioned at the tip of a micropipette by suction (Fig. 1A and 1B).

Tethered molecules were repeatedly pulled at two constant loading rates of 1.8 pN/s or 12.5 pN/s by moving up and down the optical trap along the vertical axis between fixed force limits and the resulting force-distance curves (FDCs) were recorded (Fig. 2A). A pulling cycle consists of an unfolding process and a folding process. In the unfolding process, the tethered molecule is stretched from the minimum value of force, typically in the range of 5-10 pN, where it is always at its native folded state, up to the maximum value of force, typically in the range of 25-30 pN, where the molecule is always unfolded. In the folding process the molecule is released from the higher force limit (unfolded state) up to the lower force limit (native folded state) [52]. A minimum of two molecules (different bead pairs) were tested at each ionic condition, and a minimum of 100 cycles were recorded in each case (detailed statistics are given in the Supporting Material, section S1)

2.3 Hairpin Model

Under applied force it is feasible to reduce the configurational space of an RNA hairpin containing N base pairs (bps) to a minimum set of $N+1$ partially unzipped RNA structures [36, 53, 54]. Each configuration in this set contains n adjacent opened bps in the beginning of the fork followed by $N-n$ closed bps, with $0 \leq n \leq N$. The folded state (F) is defined as the configuration in which $n = 0$ (all bps are formed), and the unfolded state (U) is the hairpin configuration in which $n = N$ (all bps are dissociated). Based on a simple calculation (see Supporting Material, section S2) we conclude that fraying [55] plays a rather minor role (if any) on the folding/unfolding kinetics of the sequence under study (Fig. 1A) and we do not include it in our analysis. The stability of each configuration n with respect to the F conformation is given by $\Delta G_{\rm n}(f)$, the free energy difference at a given force f between the duplex containing $N-n$ closed bps and the completely closed configuration (F state),

$$\Delta G_{\rm n}(f) = \Delta G_{\rm n}(0) + \Delta G_{\rm n}^{ssRNA}(f) + \Delta G_{\rm n}^{d_0}(f). \quad (1)$$

In eq. 1 $\Delta G_{\rm n}(0)$ is the free energy difference at zero force between a hairpin in the partially unzipped configuration n and a hairpin in the completely closed configuration; $\Delta G_{\rm n}^{ssRNA}(f)$ is

equal to the reversible work needed to stretch the ssRNA strands of the hairpin in configuration n ($2n$ opened bases) from a random coiled state to a force-dependent end-to-end distance $x_{\rm n}(f)$; and $\Delta G_{\rm n}^{d_0}(f)$ is the contribution related to hairpin stem orientation [56, 57]. An estimation of $\Delta G_{\rm n}(0)$ at 1M [Mon^+] can be obtained by using the nearest-neighbor (NN) energy parameters widely employed to predict the stability of RNA secondary structures [15, 19]. It is given by the sum of the stacking contributions of the duplex region, containing $N-n$ bps. The elastic term $\Delta G_{\rm n}^{ssRNA}(f)$ is given by [56]

$$\Delta G_{\rm n}^{ssRNA}(f) = -\int_0^f x_{\rm n}^{ssRNA}(f')df'. \tag{2}$$

The molecular extension of ssRNA, $x_{\rm n}^{ssRNA}(f)$, can be estimated using polymer theory (see section 2.4). Finally, the last term in eq. 1, $\Delta G_{\rm n}^{d_0}(f)$, is equal to the free energy of orientation of a monomer of length d_0 along the force axis [57]:

$$\Delta G_{\rm n}^{d_0}(f) = k_{\rm B}T \log\left[\frac{k_{\rm B}T}{f d_0}\sinh\left(\frac{f d_0}{k_{\rm B}T}\right)\right] \tag{3}$$

where f is the applied force, $k_{\rm B}$ is the Boltzmann constant, T is the bath temperature, and d_0 is the diameter of a double stranded chain, taken equal to 2 nm.

2.4 Elastic models of ssRNA

To model the elastic response of ssRNA we employed both the interpolation formula for the inextensible Worm Like Chain (WLC) model and the Freely Jointed Chain (FJC) model, which give the equilibrium end-to-end distance x of a polymer of contour length $l_{\rm n}$ stretched at a given force f. These models have been mainly tested for long polymers. However, several studies indicate that they are generally applicable when the contour length is larger than the persistence length. The inextensible WLC is given by:

$$f = \frac{k_{\rm B}T}{P}\left[\frac{1}{4\left(1-x/l_{\rm n}\right)^2} - \frac{1}{4} + \frac{x}{l_{\rm n}}\right] \tag{4}$$

where $k_{\rm B}$ is the Boltzmann constant, T is the bath temperature and P is the persistence length [58, 59]. The FJC model is given by

$$x = l_{\rm n}\left[\coth\left(\frac{fb}{k_{\rm B}T}\right) - \frac{k_{\rm B}T}{fb}\right] \tag{5}$$

where b is the Kuhn length.

There are other models, such as the Thick Chain, that are more general than the WLC or the FJC and that have been used to fit the elastic response of biopolymers. Despite of their greater complexity, we do not expect a qualitative improvement of our results by using them.

2.5 Kinetic Analysis

We applied Kramers rate theory [60] to study the kinetics of the transition between states F and U. The framework for understanding the effect of an external force on rupture rates was first introduced in [61] and extended to the case where the loading force increases with time [62, 63]. The assumption that the transition state does not move under an applied force f can be relieved by considering that the effective barrier that must be crossed by a Brownian particle is force-dependent, $B_{\text{eff}}(f)$. The unfolding and folding rates can be obtained as the first passage rates over the effective barrier,

$$k_U(f) = k_0 \exp\left(-\frac{B_{\text{eff}}(f)}{k_{\text{B}}T}\right), \tag{6a}$$

$$k_F(f) = k_0 \exp\left(-\frac{B_{\text{eff}}(f) - \Delta G_{\text{N}}(f)}{k_{\text{B}}T}\right). \tag{6b}$$

In eq. 6, F was selected as the reference state and $\Delta G_{\text{N}}(f)$ has been defined in eq. 1. k_0 is the attempt rate for activated kinetics. The effective barrier $B_{\text{eff}}(f)$ can be obtained analytically from Kramers rate theory (KT) [64, 65] (detailed derivation provided in the Supporting Material, section S3) as

$$B_{\text{eff}}^{KT}(f) = k_{\text{B}}T \log\left[\sum_{n=0}^{N} h(n) \exp\left(\frac{\Delta G_{\text{n}}(f)}{k_{\text{B}}T}\right)\right] \tag{7}$$

with $h(n) = \sum_{n'=0}^{n} \exp\left(-\frac{\Delta G_{\text{n}'}(f)}{k_{\text{B}}T}\right)$. Importantly, the location of the barrier along the reaction coordinate can be obtained from the first derivatives of $B_{\text{eff}}(f)$ with respect to force,

$$x_{\text{eff}}^{F}(f) = -\frac{dB_{\text{eff}}(f)}{df}, \tag{8a}$$

$$x_{\text{eff}}^{U}(f) = \frac{d[B_{\text{eff}}(f) - \Delta G_{\text{N}}(f)]}{df} \tag{8b}$$

where $x_{\text{eff}}^{F}(f)$ and $x_{\text{eff}}^{U}(f)$ are the distances from the effective barrier to the F and U states, respectively. The force-dependent fragility parameter $\mu(f)$ [36],

$$\mu(f) = \frac{x_{\text{eff}}^{F}(f) - x_{\text{eff}}^{U}(f)}{x_{\text{eff}}^{F}(f) + x_{\text{eff}}^{U}(f)} \tag{9}$$

lies in the range [-1:1] and is a measure of the compliance of a molecule under the effect of tension. Compliant structures deform considerably before the transition event and are characterized by positive values of $\mu(f)$, i.e. $x_{\text{eff}}^{F}(f) > x_{\text{eff}}^{U}(f)$. In contrast, brittle structures are defined by negative values of $\mu(f)$, $x_{\text{eff}}^{F}(f) < x_{\text{eff}}^{U}(f)$. A given sequence can display different fragilities at different force regimes, due to changes in the location of the transition state (TS) with force.

From the measured transition rates (see section 2.6) we can get estimators for the effective barrier $B_{\text{eff}}^{(U/F)}(f)$ for unfolding and folding using the expressions in eq. 6:

$$\frac{B_{\text{eff}}^{(U)}(f)}{k_{\text{B}}T} = -\log k_U(f) + \log k_0, \tag{10a}$$

$$\frac{B_{\text{eff}}^{(F)}(f)}{k_{\text{B}}T} = -\log k_F(f) + \log k_0 + \frac{\Delta G_{\text{N}}(f)}{k_{\text{B}}T}. \tag{10b}$$

By comparing the experimental estimators of the kinetic barrier $B_{\text{eff}}^{(U/F)}(f)$ with the effective barrier $B_{\text{eff}}^{KT}(f)$ as predicted by Kramers rate theory (eq. 7) we can extract the free energy of formation of the hairpin $\Delta G_{\text{N}}(0)$, the attempt rate k_0 and the parameters that characterize the elastic response of the ssRNA [36]. While k_0 always can be determined by doing this comparison, there is a trade-off between the contributions of the elastic response of the ssRNA and the free energy of formation of the hairpin. Although this is not strictly true (the stretching contribution term is force dependent whereas the free energy of formation term is not) it holds to a very good degree. Therefore, if only the free energy of formation of the hairpin is known *a priori*, then we can extract the elastic properties of the ssRNA by matching eqs. 10a and 10b with eq. 7. On the contrary, if we only know the elastic properties of the ssRNA, then we can extract the free energy of formation of the hairpin (see Supporting Material, section S4).

2.6 Data Analysis

The molecular transitions during unfolding and folding can be identified as force rips in a force-distance curve (FDC) [56]. In order to extract the unfolding and folding rates (eq. 6a and 6b) from experiments we have collected the first rupture forces associated with the unfolding and folding parts of each pulling cycle (Fig. 2A and 2B). By plotting the number of trajectories in which the molecule remained at the initial configuration (F state during the stretching part and U state in the releasing part of the cycle) as a function of force $N(f_i)$, divided by the total number of trajectories N_0, we obtained experimental estimators for survival probabilities $P_{U/F}(f_i) = N(f_i)/N_0$ of the U and F states. Moreover, we obtained an experimental estimator for the probability densities $\rho_{U/F}(f)$ of unfolding and folding first rupture forces by doing normalized histograms of both datasets ($\rho_{U/F}(f) = \Delta N/(\Delta f \times N_0)$, where ΔN is the number of events in the range between f and $f + \Delta f$). The survival probabilities are related to $\rho_{U(F)}(f)$ by the following equations,

$$P_U(f) = 1 - \int_{f_{min}}^{f} \rho_U(f')\mathrm{d}f', \tag{11a}$$

$$P_F(f) = 1 - \int_{f}^{f_{max}} \rho_F(f')\mathrm{d}f'. \tag{11b}$$

If we assume a two-state transition, the time-evolution of the survival probabilities is described by the following master equations [66]:

$$\frac{\mathrm{d}P_U(f(t))}{\mathrm{d}t} = -k_U(f(t))P_U(f(t)), \tag{12a}$$

$$\frac{\mathrm{d}P_F(f(t))}{\mathrm{d}t} = -k_F(f(t))P_F(f(t)). \tag{12b}$$

With this assumption and the experimental estimators for survival probabilities and densities, it is possible to extract the transition rates $k_{U(F)}(f)$ from rupture force measurements using $k_{U(F)}(f) = -r\rho_{U(F)}(f)/P_{U(F)}(f)$, with r the pulling speed [36, 56, 66].

2.7 Salt corrections

It is interesting to experimentally measure the effect of salt on the free energy of formation of nucleic acid hairpins. However, UV absorbance experiments cannot be carried out for this particular sequence because its melting temperature is too high to obtain reliable results (see Supporting Material, section S5). Therefore, as mentioned in section 2.3, the estimation of the free energy of formation of the RNA hairpin at 1M [Mon^+] is obtained using the NN energy parameters proposed by [15, 19]. To introduce the effect of monovalent salt concentration [Mon^+] we assume a sequence-independent correction $g_1([\mathrm{Mon}^+])$ for the free energy of formation of one base pair. As the free energy is measured relative to the F state we get for the free energy correction of a hairpin with n unzipped bps:

$$\Delta G_{\mathrm{n}}^{[\mathrm{Mon}^+]}(0) = \Delta G_{\mathrm{n}}^{1M}(0) - n g_1([\mathrm{Mon}^+]) \tag{13}$$

where $\Delta G_{\mathrm{n}}^{1M}(0)$ corresponds to the free energy of formation of the n^{th} configuration at 1000 mM [Mon^+] at zero force. In the case of mixed monovalent/Mg^{2+} conditions we add a second sequence-independent correction term $g_2([\mathrm{Mon}^+])$ that captures the effect of Mg^{2+} ions on the hairpin free energy of formation:

$$\Delta G_{\mathrm{n}}^{[\mathrm{Mon}^+],[\mathrm{Mg}^{2+}]}(0) = \Delta G_{\mathrm{n}}^{1M}(0) - n g_1([\mathrm{Mon}^+]) - n g_2([\mathrm{Mg}^{2+}]). \tag{14}$$

In what follows, unless stated otherwise, all monovalent and divalent salt concentrations $[\mathrm{Mon}^+], [\mathrm{Mg}^{2+}]$ are expressed in mM units.

3 Results

3.1 Effect of force on thermodynamics and kinetics of an RNA hairpin

We pulled the RNA hairpin at loading rates of 1.8 pN/s and 12.5 pN/s in buffers containing different ionic conditions (see Materials and Methods, section 2.2). From the unfolding and folding FDC we measured the first rupture forces along many cycles. The resulting probability distributions at each pulling speed and ionic condition can be found in the Supporting Material (section S6). As previously observed [36], this hairpin displays a two-state behavior, with force

jumps signaling the transition between F and U states (Fig. 2A) and with no evidence of fraying or intermediate states (see Supporting Material, section S2).

The order of magnitude of the resulting rupture forces and hysteresis effects are compatible with previous force-melting experiments carried out for other simple nucleic acid structures, like P5ab and TAR RNA hairpins [31, 32, 33] or short DNA hairpins [55]. Moreover, results at 1 M [Na^+] were in significant agreement with solution predictions [15, 73]. As expected, hysteresis effects strongly depend on the loading rate, being lower at 1.8 pN/s and higher at 12.5 pN/s. This can be seen from the experimental distributions of unfolding and folding first rupture forces (Fig. 2B), which are closer for pulling cycles performed at 1.8 pN/s.

3.2 Experiments at different monovalent cation concentrations

We performed pulling experiments at four different NaCl concentrations (see Materials and Methods, section 2.2). We find that the RNA duplex stability increases at higher [Mon^+] concentrations. For instance, rupture force distributions are displaced to higher forces (Fig. 3A) as we increase the concentration of NaCl. The greater duplex stability at higher salt concentrations can also be observed as an increase in the mean rupture force with the logarithm of the salt concentration (Fig. 3B). The standard deviation of rupture unfolding (folding) forces, that are known to be proportional to $k_BT/x_{\rm eff}^{U(F)}(f)$ [56], remain almost constant along the salt range explored. That might denote that the position of the TS mediating the unfolding and the folding transitions does not depend on [Mon^+], despite the fact that both transitions occur at higher forces. In Fig. 3C we see that the unfolding (folding) kinetic rates decrease (increase) with the salt concentration, which again shows the stabilizing effect of salt on the RNA hairpin.

3.3 Experiments at 1M NaCl

From the current set of NN energy parameters for RNA secondary structures obtained at 1000 mM NaCl concentration we can predict the free energy of formation $\Delta G_{\rm N}(0)$ for the RNA hairpin at this particular condition using the mfold server [18, 21, 67, 68]. We get $\Delta G_{\rm N}^{\rm Mfold}(0) = 63.0$ $k_{\rm B}T$ (although our experiments were performed at 1050 mM of monovalent salt, we do not expect significant differences by comparing with the prediction at 1000 mM). By applying the kinetic method introduced in section 2.5 we can evaluate the kinetic barrier associated to the unfolding reaction $B_{\rm eff}^{KT}(f)$ and $B_{\rm eff}^{(U/F)}(f)$ for a given elastic model for the ssRNA and find the one for which the theoretical prediction by Kramers rate theory (eq. 7) best matches the experimental results (eq. 10). The procedure is shown in Fig. 4A and explained in the Supporting Material (section S4). We found the best fit to our data using the inextensible WLC model with persistence length $P = 0.75 \pm 0.05$ nm and interphosphate distance $a = 0.665$ nm/base. The free energy of formation obtained is equal to $\Delta G_{\rm N}(0) = 65.3 \pm 0.3$ $k_{\rm B}T$, in reasonable agreement with the aforementioned value for $\Delta G_{\rm N}^{\rm Mfold}(0)$.

3.4 Selection of elastic parameters: experiments with monovalent salts

In order to know $\Delta G_{\rm N}(0)$ at monovalent ionic conditions different from 1050 mM we need to know the effect of salt on the elastic contribution of ssRNA strands. The elastic behavior of single-stranded RNA (poly-U) has been studied in single-molecule stretching and fluorescence experiments carried out at various [Na^+] concentrations [69, 70, 71]. Despite the extremely different contour length of the molecules under consideration (we are dealing with 44 bases-long chain in contrast to a polynucleotide of 1500-4000 bases in [70]), we take the values for the persistence length P proposed in previous stretching experiments and add our value obtained at 1050 mM. We assume that the elastic properties of ssRNA strands are independent of sequence, which can lead to a small error in the values obtained for the elastic properties of ssRNA strands in the case of sequence-dependent behavior. In fact, a sequence-dependent elastic behavior for ssDNA strands was previously considered as a possible explanation for the specific salt corrections found for the NN energy values obtained from unzipping experiments [37]. In the inset of Fig. 5 we plot the persistence lengths versus the monovalent salt concentration. To fit the data, we employ the following dependence of P on the Debye screening length λ_D^ν,

$$P \sim \lambda_D^\nu \propto \frac{1}{[\mathrm{Mon}^+]^{\nu/2}}. \tag{15}$$

No unique scaling law can be derived, as the value of ν can be 1, 2 or <1, depending on the polymer properties [72]. We can fit all data using $\nu = 1$ but also letting ν be a free parameter, which results in a value of $\nu = 0.6 \pm 0.06$. We then interpolate both fits, in order to infer the values of P in our experimental conditions of [Mon^+] concentration (50, 150, 550 and 1050 mM), as shown in Table 1.

3.5 Monovalent salt correction to the free energies of formation of the RNA hairpin

Having obtained the elastic parameters that allow us to appropriately describe the elastic response of ssRNA strands at different [Mon^+] concentrations, we still need to characterize the effect of salt on the energies of formation of the RNA hairpin at each intermediate configuration n. It is generally assumed a sequence-independent correction to the free energies of formation of nucleic acids duplexes [73, 74, 75]. However, we have previously shown that a sequence-dependent salt correction to the NN energy parameters of DNA improves the free energy prediction of both unzipping and melting experiments [37]. Related to this, it has been found that cation concentration affects RNA stability in a sequence-dependent manner [76]. In the absence of RNA sequence-specific parameters available, we adopted a sequence-independent salt correction (eq. 13) given by $g_1([\mathrm{Mon}^+]) = m \log([\mathrm{Mon}^+]/1000)$, where [$Mon^+$] is expressed in mM units. As we will see, there are experimental and theoretical evidences that support the logarithmic effect of monovalent ions to the stability of nucleic acid hairpins.

Using this correction, the variation of $\Delta G_{\rm n}(0)$ with monovalent salt concentration depends strictly on the value of the constant m. In order to derive m from our data, we compared the estimators of $B_{\rm eff}(f)$ obtained experimentally ($B^{(U)}_{\rm eff}(f)$ and $B^{(F)}_{\rm eff}(f)$ in eq. 10) with the theoretical prediction ($B^{KT}_{\rm eff}(f)$ in eq. 7) at different values of m. In Fig. 4A-D, we see the correspondence between theory and experiments at each monovalent ion concentration. For all salt concentrations, we found the best agreement at $m = 0.10 \pm 0.01$ kcal/mol. This value agrees with the sequence-independent salt correction reported for DNA duplex oligomers in melting experiments, $m = 0.110 \pm 0.033$ kcal/mol [73, 77], and in unzipping experiments of polymeric DNA, $m = 0.104 \pm 0.010$ kcal/mol [37]. Fig. 3D summarizes all the results. At a given force we see that the height of the kinetic barrier increases with salt concentration, which again indicates that salt increases kinetically the stability of the RNA structure.

In Fig. 5 we show the dependence of the measured $\Delta G_{\rm N}(0)$ of the RNA hairpin on the monovalent ion concentration. As expected from earlier observations on DNA [39, 78, 79] and from the application of counterion condensation theory to interpret polyelectrolyte effects on equilibrium involving highly charged, locally rod-like polyelectrolytes [40, 80, 81, 82], we observe an approximately linear dependence of RNA duplex stability on the logarithm of monovalent salt concentration. Interestingly, our data can also be well-described by the empirical expressions derived in [43, 44, 45], where the TBI model is used to predict the hairpin free energies at different ionic conditions (see Supporting Material, section S7).

By deriving the effective barrier as a function of force we can measure the distance of the TS to the F and U states, $x^{F}_{\rm eff}(f)$ and $x^{U}_{\rm eff}(f)$ (eqs. 8a and 8b), and the fragility $\mu(f)$ of the molecule as a function of the applied force (eq. 9). Fig. 6 shows the two extreme cases with 50 and 1050 mM [$\rm Mon^+$] (continuous and dashed lines respectively). In panel A we observe that the location of the TS changes as a function of force. The same trend is observed for the fragility in panel B, where the experimentally measured points, the predicted force-dependent fragility (black curves), and the expected values of the fragility for all possible locations n of the TS along the stem of the hairpin are represented (horizontal grid, right scale). At low forces, the TS is located near the loop, $n = 19 \pm 1$ (Fig. 6A, dark gray curves). At intermediate forces that depend on salt concentration the TS moves to the stem region $n = 6 \pm 1$ (Fig. 6A, gray curves). At large forces the TS has disappeared. These results are in agreement with previous findings using the same hairpin sequence [36]. Moreover, we see that at higher monovalent salt concentrations the locations of the different TS mediating unfolding and refolding are the same ($n \simeq 18$, 6 or 0 for low, intermediate and high forces respectively) but shifted to larger forces. These results agree with the Hammond's postulate [83]: at increasing [$\rm Mon^+$] the F state is increasingly stabilized while the TS is shifted towards the U state; simultaneously, as force increases the TS approaches the F state.

3.6 Experiments in mixed monovalent/Mg^{2+}conditions

We have also performed pulling experiments in mixed monovalent/Mg^{2+} buffers, containing a fixed concentration of $Tris^{+}$ ions (50 mM) and varying concentrations of Mg^{2+}(see Materials and Methods, section 2.2). The rupture force distributions for all mixed monovalent/Mg^{2+} conditions can be found as Supporting Material (section S6). We found two regimes in the behavior of the average rupture forces for unfolding and folding processes along the range of $[Mg^{2+}]$ experimentally explored. Below 0.1 mM $[Mg^{2+}]$, there is no significant difference between control (no Mg^{2+} added) and magnesium-containing conditions (Figs. 7A and 7B). However, at higher magnesium concentrations, we found a linear dependence of average rupture forces with the logarithm of $[Mg^{2+}]$ (Fig. 7A and 7B). Interestingly, Owczarzy *et al.* have made a similar observation in DNA melting experiments done in mixed monovalent/Mg^{2+} conditions [51]. They found that the ratio $R = \sqrt{[Mg^{2+}]}/[Mon^{+}]$ (both salts in molar units) is a convenient parameter to determine whether divalent or monovalent ions are dominant on duplex stability. If R is less than 0.22, then monovalent ions are dominant and the presence of Mg^{2+} can be ignored. In our experiments, $R = 0.0632$ and $R = 0.2$ for the 0.01 mM and 0.1 mM $[Mg^{2+}]$ conditions, respectively. As in the case of pure monovalent ion conditions, the standard deviation of rupture forces remains almost constant and we also observed a linear dependence of $\log k_U(f)$ and $\log k_F(f)$ on the applied force for the different $[Mg^{2+}]$ tested (Fig. 7C).

In order to obtain the free energy of formation $\Delta G_{\rm N}(0)$ of the RNA hairpin at different magnesium concentrations, we employed the empirical expression derived in [44, 45] by applying the TBI model to predict the RNA helix stability in mixed monovalent/Mg^{2+} ionic conditions (see Fig. 9, inset). Using this mixed salt correction, it is possible to obtain the sequence-independent correction of one base pair $g_2([Mg^{2+}])$ at any mixed salt condition using eq. 14:

$$g_2([Mg^{2+}]) = \frac{1}{N}\left(\Delta G_{\rm N}^{\rm Mfold}(0) - \Delta G_{\rm N}^{\rm TBI}(0) - Nm\log([Mon^{+}/1000])\right). \qquad (16)$$

From this expression, we can extract the value of $\Delta G_{\rm n}^{[Mon^{+}],[Mg^{2+}]}(0)$ in eq. 14 for any intermediate state n. By varying the mixed salt-dependent values for the persistence length P of the ssRNA for each $[Mg^{2+}]$, we can now determine the value of P that results in better agreement between the predicted effective barrier $B_{\rm eff}^{KT}(f)$ and our experimental estimations (Fig. 8 and Supporting Material, section S4). All the results are summarized in Fig. 7D, where we can see that the stability of the hairpin increases with magnesium concentration. The dependence of P on $[Mg^{2+}]$ is shown in Fig. 9. Table 2 summarizes the results obtained for the persistence length P and the attempt frequency k_0. The position of the TS varied with $[Mg^{2+}]$ in a way similar to what we found for $[Mon^{+}]$. In a specified force the TS mediating the unfolding and folding transitions is shifted toward the U state as the $[Mg^{2+}]$ is raised (Fig. 10A), in agreement with the Hammond's postulate [83]. The force-dependence of the position of the TS with respect to the F state $x_{\rm eff}^{F}(f)$ and the hairpin fragility $\mu(f)$ are similar in both monovalent and mixed ionic conditions (Figs. 6A, B and 10A, B). At low forces the TS is located near the loop, whereas at

intermediate forces it is located in the stem region $n = 6 \pm 1$ (Fig. 10A, B).

4 Discussion

The effect of monovalent ion concentration on DNA stability has been extensively studied and there is a variety of empirical salt corrections available in the literature [84, 85]. There is no general agreement about the accuracy and limitations of use of salt corrections in terms of sequence length and range of salt concentrations [84]. Recently, we have reported 10 NN salt correction parameters for prediction of DNA duplex stability derived from single-molecule experiments [37]. However, there is no equivalent study on RNA duplexes and the experimental data available for the salt effects on RNA duplex stability are limited to short sequences that display a two-state behavior [76]. Different polyelectrolyte theories try to characterize the interaction between counterions and nucleic acids to study ionic effects to the molecular stability. The most accepted are mean field theories such as the Poison-Boltzmann and the counterion condensation theories [80, 81]. Recently, the Tightly Bound Ion (TBI) model has been proposed [43]. It incorporates correlation and fluctuation effects for bound ions, and has been extended to treat RNA helices under mixed monovalent/divalent salt conditions [44, 45]. It was shown that the TBI improves the prediction of the stabilities of RNA duplexes smaller than 15 bp [44, 86].

Here, we performed a detailed characterization of the effect of monovalent and mixed monovalent/magnesium concentrations on the stability of a RNA hairpin containing a stem of 20 bp by mechanically unfolding and folding the molecule using optical tweezers. The results we have obtained can be very well described by the empirical formulas derived from the TBI model for predicting the stabilities of RNA hairpins in monovalent ion and mixed monovalent/Mg^{2+} buffer conditions. A comparison of the counterion condensation theory [87] is provided in the Supporting Material (section S8), and although an acceptable accuracy is found at monovalent salt conditions, we observe that correlation effects become important in the presence of Mg^{2+} ions and therefore the TBI gives improved predictions.

When a hairpin is melted mechanically the U state is subjected to a tension. In standard optical melting and calorimetric experiments, the U state is under zero force. Therefore, to appropriately compare both phenomena, it is necessary to discount the energy required to stretch the single stranded unfolded state in mechanical experiments. However, we have limited information about the elastic properties of single stranded RNA as compared to DNA. Despite the chemical similarity between both polymers, the RNA-specific 2'-OH group favors a conformationally restricted $C3' - endo$ structure [88]. Moreover, in previous single-molecule studies [69, 71], the elastic response of a single-stranded poly-U RNA was better described by a WLC model rather than by a FJC model. Based on these considerations, we decided to use the numbers derived from single-molecule stretching experiments for the elastic behavior of ssRNA molecules (as explained in section 3.2) to appropriately account for the energetic contribution of stretching the ssRNA strands during mechanical unfolding.

By applying the Kramers rate theory and correctly accounting for the elastic contribution of ssRNA stretching we were able to obtain the free energy of formation of the RNA hairpin from pulling experiments done in non-equilibrium conditions. This allowed us to obtain a large number of trajectories at different ionic conditions in a feasible timescale. In this way, we obtained the effective barrier of the unfolding reaction as a function of force for different ionic conditions.

The ability of Mg^{2+} ions to stabilize RNA structures at much lower concentrations than monovalent ions was recognized almost forty years ago [89]. In fact, by plotting the values of the free energies of formation versus salt concentration (expressed in mM units) we can collapse data for both types of salt into a single master curve by multiplying $[Mg^{2+}]$ by a factor 100 (Fig. 11A). This effect has been previously observed [24, 46, 47, 90, 91] and can be explained using the counterion condensation theory which account for strong correlations between counterions and polyelectrolytes [46, 81, 82, 92]. A similarity (but not a data collapse) is obtained for the persistence length values of ssRNA (Fig. 11B). It can be interpreted as the screening effect of the counterions present in solution: the longer the screening length, the stiffer the molecule. This equivalence found between the non-specific binding of monovalent and divalent salts with nucleic acids might be useful to develop new biochemical assays in situations where divalent ion-specific interactions could be detrimental [93].

As a further step, it would be very interesting to extend this study by mechanically unfolding an RNA hairpin containing a Mg^{2+}-specific binding site using our experimental setup. Eventually, the energetic contributions of different specific binding sites could be dissected and incorporated into current models of RNA structure prediction.

5 Supporting material

Supporting material is available at NAR Online.

6 Funding

This work was supported by the Human Frontier Science Program (RGP55-2008); the Institució Catalana de Recerca i Estudis Avançats; the Centro de Investigación Biomédica en Red en Bioingeniería, Biomateriales y Nanomedicina; and the Spanish Ministerio de Educación-Ministerio de Ciencia e Innovación (AP2007-00995 to A. A., FIS2011-19342 to F. R.).

Acknowledgements

We acknowledge I. Tinoco, M. Manosas and A. Bosco for a careful reading of the manuscript; We also acknowledge R. Eritja and A. Aviñó for their advice and help in carrying out the UV absorbance measurements.

References

[1] Berkhout B., Silverman R.H. and Jeang K.T. (1989) Tat trans-activates the human immunodeficiency virus through a nascent RNA target. *Cell* **59(2),** 273-282.

[2] Olsthoorn R.C.L., Mertens S., Brederode F.T. and Bol J.F. (1999) A conformational switch at the 3' end of a plant virus RNA regulates viral replication. *EMBO J.* **18(17),** 4856-4864.

[3] Gollnick P., Babitzke P., Antson A. and Yanofsky C. (2005) Complexity in Regulation of Tryptophan Biosynthesis in Bacillus subtilis. *Annu. Rev. Genet.* **39,** 47-68.

[4] Garst A.D. and Batey R.T. (2009) A switch in time: Detailing the life of a riboswitch. *Biochim. Biophys. Acta* **1789(9-10),** 584-591.

[5] Li L. and Liu Y. (2011) Diverse Small Non-coding RNAs in RNA Interference Pathways. *Methods in Molecular Biology* **764,** 169-182.

[6] Kawaji,H. and Hayashizaki,Y. (2008) Exploration of small RNAs. *PLoS Genet.* **4(1),** e22.

[7] Zhang,J., Lau,M. and Ferré-D'Amaré,A. (2010) Ribozymes and riboswitches: modulation of RNA function by small molecules. *Biochemistry* **49,** 9123-9131.

[8] Bardaro Jr, M.F., Shajani, Z., Patora-Komisarska, K., Robinson, J.A. and Varani, G. (2009) How binding of small molecule and peptide ligands to HIV-1 TAR alters the RNA motional landscape. *Nucl. Acids Res.* **37,** 1529-1540.

[9] Tinoco Jr I. and Bustamante C. (1999) How RNA Folds. *J. Mol. Biol.* **293,** 271-281.

[10] Zhao, P., Zhang, W.-B. and Chen, S.-J. (2010) Predicting Secondary Structural Folding Kinetics for Nucleic Acids. *Biophys. J.* **98,** 1617-1625.

[11] Chen S.J. and Dill K.A. (2000) RNA folding energy landscapes. *Proc. Natl. Acad. Sci. U. S. A.* **97(2),** 646-51.

[12] Hyeon C. and Thirumalai D. (2006) Forced-unfolding and force-quench refolding of RNA hairpins. *Biophys J.* **90(10),** 3410-27.

[13] Petesheim,M. and Turner,D.H. (1983) Base-stacking and base-pairing contributions to helix stability: thermodynamics of double-helix formation with CCGG, CCGGp, CCGGAp, ACCGGp, CCGGUp, and ACCGGUp. *Biochemistry* **22,** 256-263.

[14] Freier,S.M., Kierzek,R., Jaeger,J.A., Sugimoto,N., Caruthers,M.H., Neilson, T. and Turner,D.H. (1986) Improved free-energy parameters for predictions of RNA duplex stability. *Proc. Natl. Acad. Sci. U.S.A.* **83,** 9373-9377.

[15] Walter,A.E., Turner,D.H., Kim,J., Lyttle, M.H., Müller,P., Mathews, D.H. and Zuker,M. (1994) Coaxial stacking of helixes enhances binding of oligoribonucleotides and improves predictions of RNA folding. *Proc. Natl. Acad. Sci. U.S.A.* **91,** 9218-9222.

[16] Serra,M.J., Axenson,T.J. and Turner,D.H. (1994) A model for the stabilities of RNA hairpins based on a study of the sequence dependence of stability for hairpins of six nucleotides. *Biochemistry* **33,** 14289-14296.

[17] Serra,M.J., Barnes,T.W., Betschart,K., Gutierrez,M.J., Sprouse,K.J., Riley, C.K., Stewart,L. and Temel,R.E. (1997) Improved parameters for the prediction of RNA hairpin stability. *Biochemistry* **36,** 4844-4851.

[18] Xia,T., SantaLucia Jr.,J., Burkard,M.E., Kierzek,R., Schroeder,S.J., Jiao,X., Cox,C. and Turner,D.H. (1998) Thermodynamic parameters for an expanded nearest-neighbor model for formation of RNA duplexes with Watson-Crick base pairs. *Biochemistry* **37,** 14719-14735.

[19] Mathews,D.H., Sabina,J., Zuker,M. and Turner,D.H. (1999) Expanded sequence dependence of thermodynamic parameters improves prediction of RNA secondary structure. *J. Mol. Biol.* **288,** 911-940.

[20] Znosko,B.M., Silvestri,S.B., Volkman,H., Boswell,B. and Serra,M.J. (2002) Thermodynamic parameters for an expanded nearest-neighbor model for the formation of RNA duplexes with single nucleotide bulges. *Biochemistry* **41,** 10406-10417.

[21] Mathews,D.H., Disney,M.D., Childs,J.L., Schroeder,S.J., Zuker,M. and Turner,D.H. (2004) Incorporating chemical modification constraints into a dynamic programming algorithm for prediction of RNA secondary structure. *Proc. Natl. Acad. Sci. U.S.A.* **101,** 7287-7292.

[22] Fürtig,B., Wenter,P., Reymond,L., Richter,C., Pitsch,S., and Schwalbe,H. (2007) Conformational dynamics of bistable RNAs studied by time-resolved NMR spectroscopy. *J. Am. Chem. Soc.* **129,** 16222-16229.

[23] Fürtig B., Wenter P., Pitsch S. and Schwalbe H. (2010) Probing mechanism and transition state of RNA refolding. *ACS Chem Biol.* **5(8),** 753-65.

[24] Williams,A.P., Longfellow,C.E., Freier,S.M., Kierzek,R. and Turner,D.H. (1989) Laser Temperature-Jump, Spectroscopic, and Thermodynamic Study of Salt Effects on Duplex Formation by dGCATGC. *Biochemistry* **28,** 4283-4291.

[25] Ma H., Proctor D.J., Kierzek E., Kierzek R., Bevilacqua P.C. and Gruebele M. (2006) Exploring the energy landscape of a small RNA hairpin. *J. Am. Chem. Soc.* **128(5),** 1523-30.

[26] Sarkar K., Meister K., Sethi A. and Gruebele M. (2009) Fast folding of an RNA tetraloop on a rugged energy landscape detected by a stacking-sensitive probe. *Biophys. J.* **97(5),** 1418-27.

[27] Sarkar K., Nguyen D.A. and Gruebele M. (2010) Loop and stem dynamics during RNA hairpin folding and unfolding. *RNA* **12,** 2427-34.

[28] Stancik A.L. and Brauns E.B. (2008) Rearrangement of partially ordered stacked conformations contributes to the rugged energy landscape of a small RNA hairpin. *Biochemistry* **47(41),** 10834-40.

[29] Zhang W. and Chen S.J. (2006) Exploring the complex folding kinetics of RNA hairpins: I. General folding kinetics analysis. *Biophys. J.* **90(3),** 765-77.

[30] Hyeon C. and Thirumalai D. (2005) Mechanical unfolding of RNA hairpins. *Proc. Natl. Acad. Sci. U. S. A.* **102(19),** 6789-94.

[31] Liphardt, J., Onoa, B., Smith, S.B., Tinoco Jr., I. and Bustamante, C. (2001) Reversible Unfolding of Single RNA Molecules by Mechanical Force. *Science* **292,** 733-737.

[32] Tinoco Jr, Collin D. and Li P.T.X. (2004) The effect of force on thermodynamics and kinetics: unfolding single RNA molecules. *Biochem. Soc. Trans.* **32(Pt 5),** 757-760.

[33] Li, P.T., Collin, D., Smith, S.B., Bustamante, C. and Tinoco, I. Jr (2006) Probing the mechanical folding kinetics of TAR RNA by hopping, force-jump, and force-ramp methods. *Biophys. J.* **90,** 250-260.

[34] Bustamante C., Chemla Y.R., Forde N.R. and Izhaky D. (2004) Mechanical processes in biochemistry. *Annu. Rev. Biochem.* **73,** 705-48.

[35] Tinoco,I., Chen,G. and Qu,X. (2010) RNA reactions one molecule at a time. *Cold Spring Harb. Perspect. Biol.* **2,** a003624.

[36] Manosas,M., Collin,D. and Ritort,F. (2006) Force-dependent fragility in RNA hairpins. *Phys. Rev. Lett.* **96,** 218301.

[37] Huguet,J.M., Bizarro,C.V., Forns,N., Smith,S.B., Bustamante,C. and Ritort, F. (2010) Single-molecule derivation of salt dependent base-pair free energies in DNA. *Proc. Natl. Acad. Sci. U.S.A.* **107,** 15431-15436.

[38] Bustamante,C. and Smith,S.B. (2006) Patent US 7133132 B2.

[39] Record, M. Th., Jr. (1975). Effects of Na^+ and Mg^{2+} ions on the helix-coil transition of DNA. *Biopolymers* **14,** 2137-2158.

[40] Record Jr., M. T., Woodbury, C. P. and Lohman, T. M. (1976) Na+ effects on transitions of DNA and polynucleotides of variable linear charge density. *Biopolymers* **15(5),** 893-915.

[41] Williams,D.J. and Hall,K.B. (1996) Thermodynamic comparison of the salt dependence of natural RNA hairpins and RNA hairpins with non-nucleotide spacers. *Biochemistry* **35,** 14665-14670.

[42] Takach,J., Mikulecky,P. and Feig,A. (2004) Salt-dependent heat capacity changes for RNA duplex formation. *J. Am. Chem. Soc. 126(21),* 6530-6531.

[43] Tan,Z.J. and Chen,S.J. (2005) Electrostatic correlations and fluctuations for ion binding to a finite length polyelectrolyte. *J. Chem. Phys.* **122(4),** 44903.

[44] Tan,Z.J. and Chen,S.J. (2007) RNA helix stability in mixed Na^+/Mg^{2+} solution. *Biophys. J.* **92,** 3615-3632.

[45] Tan,Z.J. and Chen,S.J. (2008) Salt dependence of nucleic acid hairpin stability. *Biophys. J.* **95,** 738-752.

[46] Heilman-Miller, S. L., Thirumalai, D. and Woodson, S. A. (2001) Role of Counterion Condensation in Folding of Tetrahymena Ribozyme. I: Equilibrium Stabilization by Cations. *J. Mol. Biol.* **306,** 1157-1166.

[47] Z. J. Tan and S. J. Chen (2009) Predicting Electrostatic Forces in RNA Folding *Methods in Enzymology* **469,** Chapter 22.

[48] Collin,D., Ritort,F., Jarzynski,C., Smith,S.B., Tinoco Jr,I. and Bustamante, C. (2005) Verification of the Crooks fluctuation theorem and recovery of RNA folding free energies. *Nature* **437,** 231-234.

[49] McManus,M.T., Petersen,C.P., Haines,B.B., Chen,J. and Sharp,P.A. (2002) Gene silencing using micro-RNA designed hairpins. *RNA* **8,** 842-850.

[50] Casey,J. and Davidson, N. (1977) Rates of formation and thermal stabilities of RNA:DNA and DNA:DNA duplexes at high concentrations of formamide. *Nucleic Acids Res.* **4,** 1539-1552.

[51] Owczarzy,R., Moreira,B.G., You,Y., Behlke,M.A. and Walder,J.A. (2008) Predicting stability of DNA duplexes in solutions containing magnesium and monovalent cations. *Biochemistry* **47,** 5336-5353.

[52] Liphardt,J., Dumont,S., Smith,S.B., Tinoco,I. and Bustamante,C. (Jun, 2002) Equilibrium information from nonequilibrium measurements in an experimental test of Jarzynski's equality. *Science* **296(5574),** 1832-1835.

[53] Cocco,S., Marko,J.F. and Monasson,R. (2003) Slow nucleic acid unzipping kinetics from sequence-defined barriers. *Eur. Phys. J. E: Soft Matter Biol. Phys.* **10,** 153-161.

[54] Manosas,M. and Ritort,F. (2005) Thermodynamic and kinetic aspects of RNA pulling experiments. *Biophys. J.* **88,** 3224-3242.

[55] Woodside M.T., Anthony P.C., Behnke-Parks W.M., Larizadeh K., Herschlag D. and Block S.M. (2006) Direct measurement of the full, sequence-dependent folding landscape of a nucleic acid. *Science* **314(5801),** 1001-4.

[56] Mossa,A., Manosas,M., Forns,N., Huguet,J.M. and Ritort,F. (2009) Dynamic force spectroscopy of DNA hairpins: I. Force kinetics and free energy landscapes. *J. Stat. Mech.* P02060.

[57] Forns,N., de Lorenzo,S., Manosas,M., Hayashi,K., Huguet,J.M. and Ritort, F. (2011) Improving signal/noise resolution in single-molecule experiments using molecular constructs with short handles. *Biophys. J.* **100(7),** 1765-1774.

[58] Bustamante,C., Marko,J.F., Siggia,E.D. and Smith,S. (1994) Entropic elasticity of lambda-phage DNA. *Science* **265,** 1599-1600.

[59] Marko,J.F. and Siggia,E.D. (1995) Stretching DNA. *Macromolecules* **28,** 8759-8770.

[60] Kramers,H.A. (1940) Brownian motion in a field of force and the diffusion model of chemical reactions. *Physica* **7,** 284-304.

[61] Bell,G.I. (1978) Models for the specific adhesion of cells to cells. *Science* **200,** 618-627.

[62] Evans,E. and Ritchie,K. (1997) Dynamic strength of molecular adhesion bonds. *Biophys. J.* **72,** 1541-1555.

[63] Qian,H. and Shapiro,B.E. (1999) Graphical Method for Force Analysis: Macromolecular Mechanics With Atomic Force Microscopy. *Proteins: Structure, Function, and Genetics* **37,** 576-581.

[64] Zwanzig,R. (2001) Nonequilibrium Statistical Mechanics, Oxford University Press, 1st edition.

[65] Hyeon, C. and Thirumalai, D. (2007) Measuring the energy landscape roughness and the transition state location of biomolecules using single molecule mechanical unfolding experiments. *J. Phys.: Condens. Matter* **19,** 113101.

[66] Evans,E., Halvorsen,K., Kinoshita,K. and Wong,W.P. (2009) A new approach to analysis of single-molecule force measurements. *Springer Science+ Business Media*

[67] Tinoco,I., Uhlenbeck,O.C. and Levine,M.D. (1971) Estimation of Secondary Structure in Ribonucleic Acids19. *Nature* **230,** 362-367.

[68] Zuker,M. (2003) Mfold server for nucleic acid folding and hybridization prediction. *Nucleic Acids Res.* **31,** 3406-3415.

[69] Seol,Y., Skinner,G.M. and Visscher,K. (2004) Elastic properties of a singlestranded charged homopolymeric ribonucleotide. *Phys. Rev. Lett.* **93,** 118102.

[70] Toan,N.M. and Micheletti,C. (2006) Inferring the effective thickness of polyelectrolytes from stretching measurements at various ionic strengths: applications to DNA and RNA. *J. Phys.: Condens. Matter.* **18,** S269-S281.

[71] Chen, H., Meisburger, S. P., Pabit, S. A., Sutton, J. L., Webb, W. W. and Pollack, L. (2012) Ionic strength-dependent persistence lengths of single-stranded RNA and DNA. *Proc. Natl. Acad. Sci. U.S.A.* **109,** 799-804.

[72] Micka,U. and Kremer,K. (1996) Persistence length of the Debye-Hückel model of weakly charged flexible polyelectrolyte chains. *Phys. Rev. E: Stat., Nonlinear, Soft Matter Phys.* **54,** 2653-2662.

[73] SantaLucia,J.J. (1998) A unified view of polymer, dumbbell, and oligonucleotide DNA nearest-neighbor thermodynamics. *Proc. Natl. Acad. Sci. U.S.A.* **95,** 1460-1465.

[74] SantaLucia,J.J. and Hicks,D. (2004) The Thermodynamics of DNA structural motifs. *Annu. Rev. Biophys. Biomol. Struct.* **33,** 415-440.

[75] Shkel,I.A. and Record,J.M.T. (2004) Effect of the number of nucleic acid oligomer charges on the salt dependence of stability (ΔG_{37^o}) and melting temperature (T_m): NLPB analysis of experimental data. *Biochemistry* **43,** 7090-7101.

[76] Vieregg,J., Cheng,W., Bustamante,C. and Tinoco,I.J. (2007) Measurement of the effect of monovalent cations on RNA hairpin stability. *J. Am. Chem. Soc.* **129,** 14966-14973.

[77] Peyret,N. (2000) Prediction of Nucleic Acid Hybridization: Parameters and Algorithms. *PhD thesis.* Wayne State University Department of Chemistry, Detroit, MI.

[78] Dove, W. F. and Davidson, N. (1962) Cation effects on the denaturation of DNA. *Journal of Molecular Biology* **5(5),** 467-478.

[79] Privalov, P. L., O. B. Ptitsyn, and T. M. Birshtein. (1969) Determination of stability of the DNA double helix in an aqueous medium. *Biopolymers* **8,** 559-571.

[80] Manning, G. S. 1972. On the application of polyelectrolyte "limiting laws" to the helix-coil transition of DNA. I. Excess univalent cations. *Biopolymers* **11,** 937-949.

[81] Manning, G. S. (1978) The molecular theory of polyelectrolyte solutions with applications to the electrostatic properties of polynucleotides. *Quart. Rev. biophys.* **11,** 179-246.

[82] Record, M. T., Jr, Anderson, C. F. and Lohmna, T. M. (1978) Thermodynamic analysis of ion effects on the binding and conformational equilibra of proteins and nucleic acids: the roles of ions association of release, secreening, and ion effects on water activity. *Quart. Rev. Biophys.* **11,** 103-178.

[83] Hammond G.S. (1955) A correlation of reaction rates. *J. Am. Chem. Soc.* **77,** 334-338.

[84] Owczarzy,R., You,Y., Moreira,B.G., Manthey,J.A., Huang,L., Behlke,M.A. and Walder,J.A. (2004) Effects of sodium ions on DNA duplex oligomers: improved predictions of melting temperatures. *Biochemistry* **43,** 3537-3554.

[85] Jost,D. and Everaers,R. (2009) A unified Poland-Scheraga model of oligoand polynucleotide DNA melting: salt effects and predictive power. *Biophys. J.* **96,** 1056-1067.

[86] Tan, Z. J. and Chen, S. J. (2006) Nucleic Acid Helix Stability: Effects of Salt Concentration, Cation Valence and Size, and Chain Length. *Biophys. J.* **90,** 1175-1190.

[87] Manning, G. S. (2002) Electrostatic free energy of the DNA double helix in counterion condensation theory. *Biphys. Chem.* **101-102,** 461-473.

[88] Rich,A. (2003) The double helix: a tale of two puckers. *Nat. Struct. Mol. Biol.* **10,** 247-249.

[89] Cole,P.E., Yang,S.K. and Crothers,D.M. (1972) Conformational changes of transfer ribonucleic acid. Equilibrium phase diagrams. *Biochemistry* **11,** 4358-4368.

[90] Schroeder,S.J. and Turner,D.H. (2000) Factors Affecting the Thermodynamic Stability of Small Asymmetric Internal Loops in RNA. *Biochemistry* **39,** 9257-9274.

[91] Shankar,N., Kennedy,S.D., Chen,G., Krugh,T.R. and Turner,D. H. (2006) The NMR Structure of an Internal Loop from 23S Ribosomal RNA Differs from Its Structure in Crystals of 50S Ribosomal Subunits. *Biochemistry* **45,** 11776-11789.

[92] Shklovskii, B. I. (1999) Screening of a macroion by multivalent ions: Correlation-induced inversion of charge. *Phys. Rev. E* **60 (5),** 5082-5811.

[93] Douglas, S.M., Dietz,H., Liedl,T., Högberg,B., Graf,F. and Shih,W.M. (2009) Self-assembly of DNA into nanoscale three-dimensional shapes. *Nature* **459,** 414-418.

[94] Cain R. J. and Glick G. D. (1997) The effect of cross-links on the conformational dynamics of duplex DNA. Nucl. Acids Res. 25(4):836-842.

[95] Arrhenius, S. (1889) On the reaction rate of the inversion of non-refined sugar upon souring. *Z Phys Chem* **4,** 226248.

[96] Tan, Z. J. and Chen, S. J. (2005) Electrostatic correlations and fluctuations for ion binding to a finite length polyelectrolyte. *J. Chem. Phys.* **122,** 044903.

7 Figure Legends

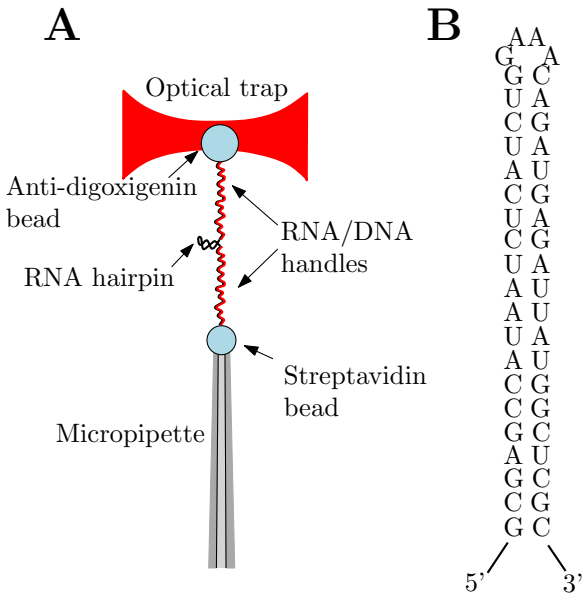

Figure 1. Experimental setup and RNA sequence. (**A**) A single RNA hairpin is attached to two polystyrene microspheres through RNA/DNA heteroduplexes used as handles. The anti-digoxigenin antibody-coated microsphere is optically trapped while the streptavidin-coated microsphere is positioned at the tip of a micropipette by air suction. (**B**) RNA hairpin sequence.

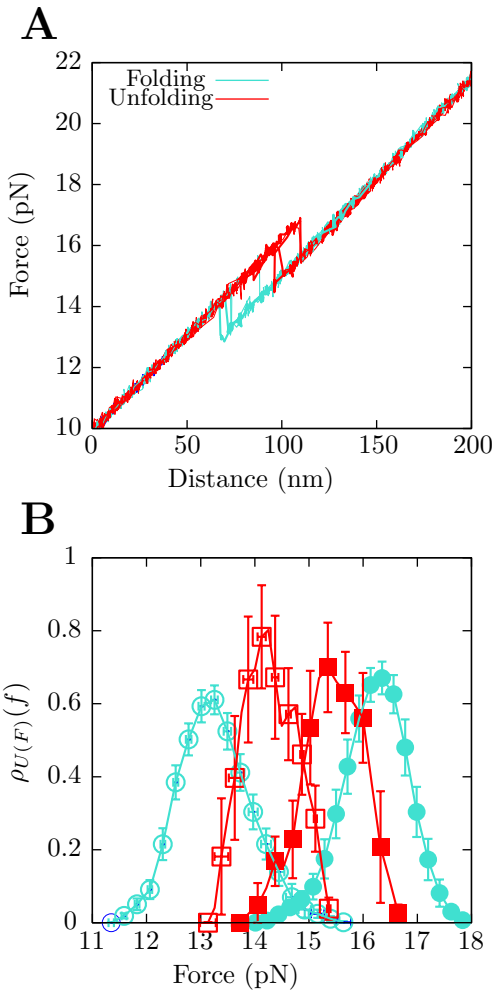

Figure 2. Pulling experiments. (**A**) A few pulling cycles for the RNA hairpin showing the unfolding (red) and folding (blue) trajectories. (**B**) Experimental distribution for the unfolding first rupture forces at 1.8 pN/s (red full squares) and 12.5 pN/s (blue full circles), and for the folding first rupture forces at 1.8 pN/s (red empty squares) and 12.5 pN/s (blue empty circles).

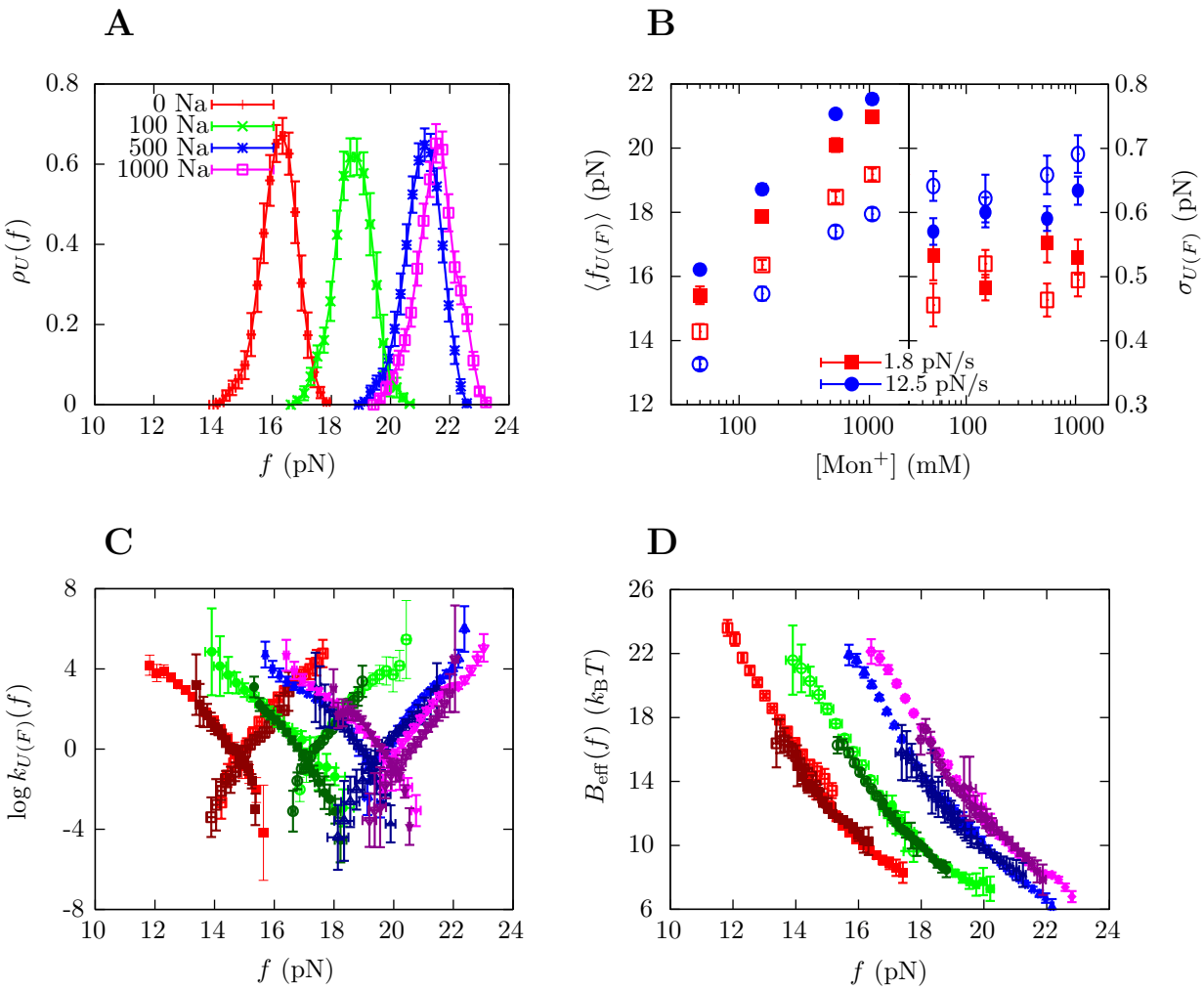

Figure 3. Kinetic analysis of experiments at varying [Mon$^+$]. (**A**) Experimental distribution of the unfolding rupture forces in buffers containing 50 mM (red), 150 mM (green), 550 mM (blue), and 1050 mM (magenta) [Mon$^+$]. These experiments were done at a loading rate of 1.8 pN/s. (**B**) Average rupture forces $\langle f_{U(F)} \rangle$ and standard deviations $\sigma_{U(F)}$ as a function of monovalent cation concentration at loading rates of 1.8 pN/s (red) and 12.5 pN/s (blue). Full symbols refer to unfolding and empty symbols to folding. (**C**) Log-Linear plot of the transition rates versus force. Experiments were done at 50 mM [Mon$^+$] for loading rates of 1.8 pN/s (dark red) and 12.5 pN/s (red), at 150 mM [Mon$^+$] for loading rates of 1.8 pN/s (dark green) and 12.5 pN/s (green), at 550 mM [Mon$^+$] for loading rates of 1.8 pN/s (dark blue) and 12.5 pN/s (blue), and at 1050 mM [Mon$^+$] for loading rates of 1.8 pN/s (dark violet) and 12.5 pN/s (magenta). (**D**) Dependence of the effective barrier $B_{\rm eff}(f)$ on force at different [Mon$^+$]. Color code as in (**C**).

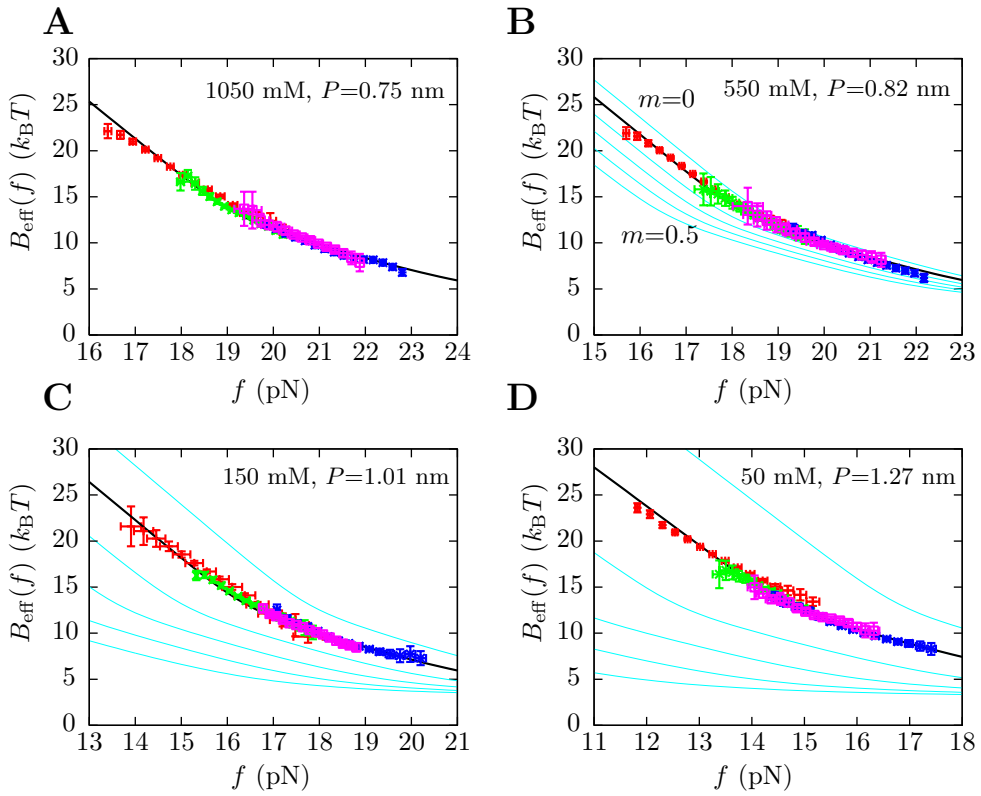

Figure 4. Determination of the salt correction parameter m. Experimental evaluation of the sequence-independent correction parameter m from $g_1([\text{Mon}^+]) = m \log([\text{Mon}^+]/1000)$ using eq. 10. Estimators of $B_{\text{eff}}^{(U/F)}(f)$ obtained experimentally (eqs. 10) were compared with the expected $B_{\text{eff}}^{KT}(f)$ (eq. 7) profiles for different values of m (0, 0.1, 0.2, 0.3, 0.4 and 0.5 from top to bottom). Red (green) points are the experimental estimators $B_{\text{eff}}^{(F)}(f)$ at a pulling rate of 12.5 (1.8) pN/s. Blue (magenta) points are the experimental estimators of $B_{\text{eff}}^{(U)}(f)$ at a pulling rate of 12.5 (1.8) pN/s. Light blue lines are the $B_{\text{eff}}^{KT}(f)$ profiles for values of m not matched, and black lines are the experimental estimators of $B_{\text{eff}}(f)$ that match with experiments. Application of the method to experiments done at 1050 mM $[\text{Mon}^+]$ (**A**), 550 mM $[\text{Mon}^+]$ (**B**), 150 mM $[\text{Mon}^+]$ (**C**), and 50 mM $[\text{Mon}^+]$ (**D**).

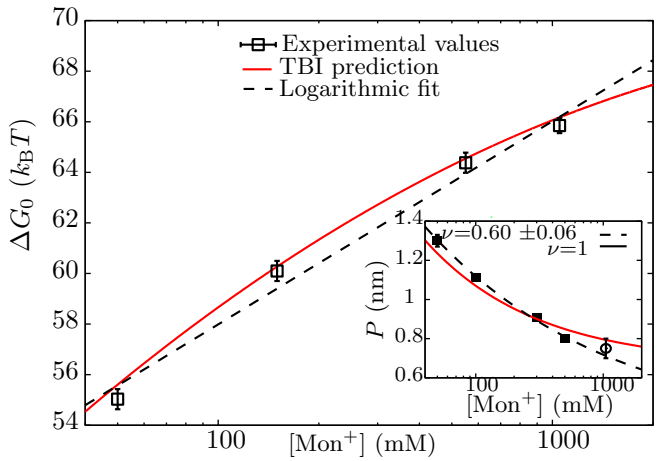

Figure 5. Free energy of formation of the RNA hairpin as a function of [Mon$^+$]. Main panel: Free energy obtained experimentally (squares), using the logarithmic dependence with salt concentration given by $g_1([\text{Mon}^+])$ (dashed line) and using the TBI model (continuous line) Inset: Persistence lengths P obtained from the application of the Thick Chain model to published experimental data for poly-U RNA stretching in buffers containing 5, 10, 50, 100, 300, and 500 mM of [Na$^+$] (squares) [69, 70]. We have included the value of the persistence length P that we obtained in this study at 1050 mM [Mon$^+$] (empty circle). Two different fits to data were done from eq. 15: a fixed value $\nu = 1$ (red) and ν as free parameter $\nu = 0.60 \pm 0.06$ (blue).

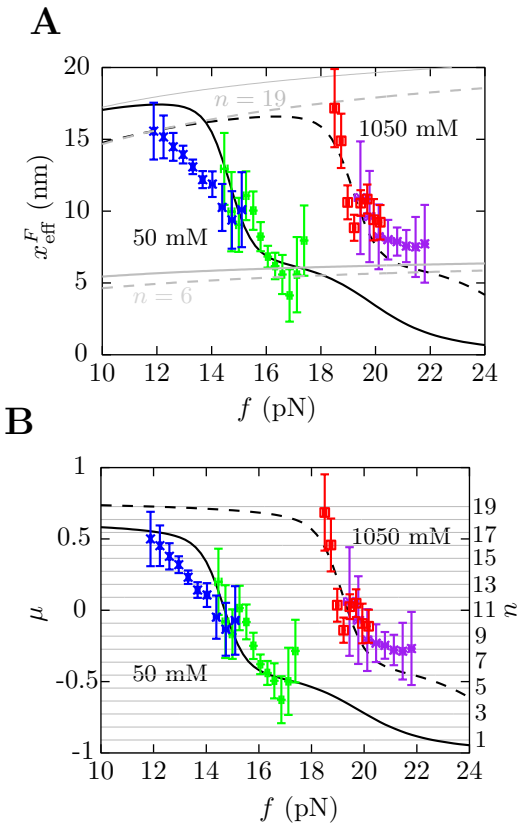

Figure 6. Barrier location and mechanical fragility at 50 mM and 1050 mM [Mon$^+$]. (**A**) Force-dependence of the barrier position measured with respect to the F state, $x_{\rm eff}^F(f)$. Continuous gray line is the WLC prediction of the molecular extension when $n = 19$ or $n = 6$ bps are unzipped at 50 mM [Mon$^+$], and dashed gray line corresponds to the WLC prediction when $n = 19$ or $n = 6$ bps are unzipped at 1050 mM [Mon$^+$]. As seen, at an intermediate value of forces $n = 6$ coincides with the TS for both ionic conditions. (**B**) Dependence of fragility $\mu(f)$ with force. Gray lines indicate the value of the fragility for different locations n of the TS along the stem. Continuous black lines are the theoretical prediction using Kramers rate theory for data at 50 mM [Mon$^+$], and dashed black lines for data at 1050 mM [Mon$^+$]. Blue and green points are the experimental evaluation of $x_{\rm eff}^F(f)$ and $\mu(f)$ for folding and unfolding data collected at 50 mM [Mon$^+$]. Red and purple points are the experimental evaluation for folding and unfolding at 1050 mM [Mon$^+$].

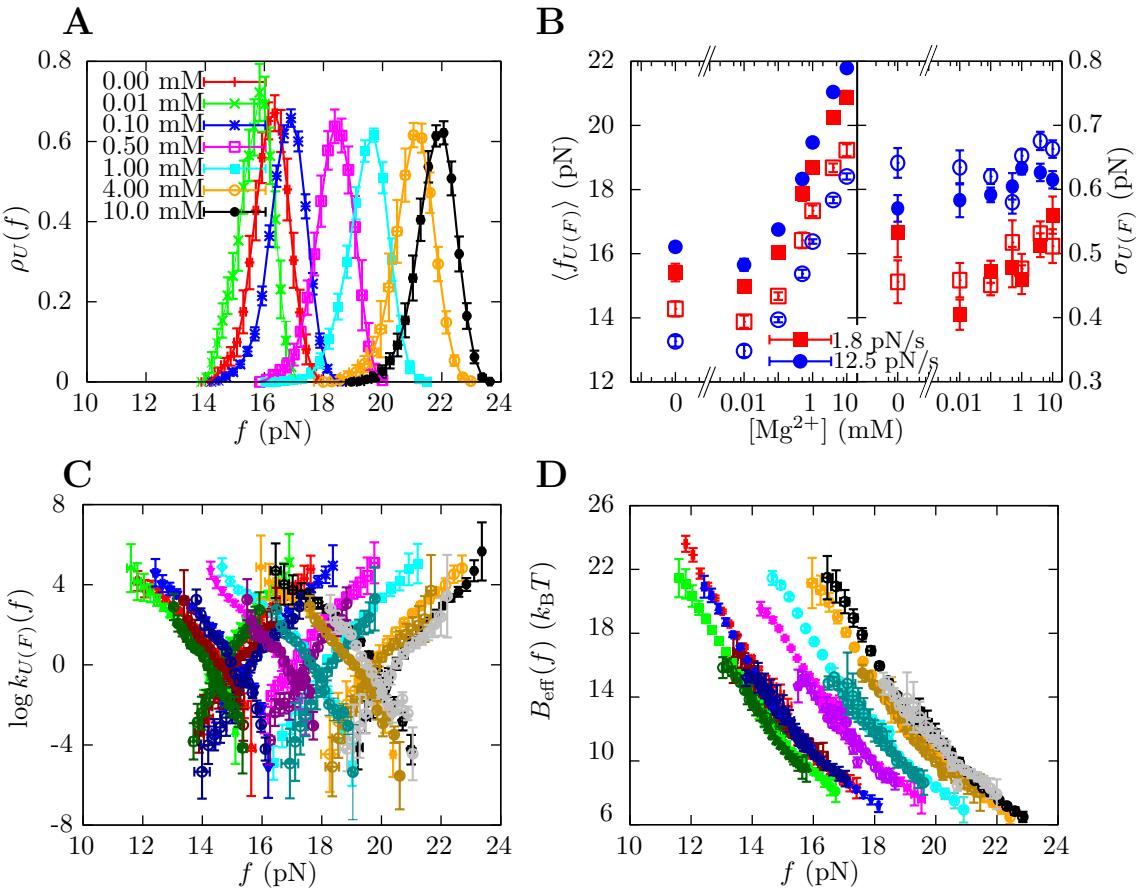

Figure 7. Kinetic analysis of experiments at varying [Mg^{2+}]. (**A**) Experimental distribution of the unfolding rupture forces in buffers containing 0.00 mM (red), 0.01 mM (green), 0.1 mM (blue), 0.5 mM (magenta), 1 mM (cyan), 4 mM (orange), and 10 mM (black) of [Mg^{2+}] and 50 mM of monovalent cations. These experiments were done at a loading rate of 1.8 pN/s. (**B**) Average rupture forces $\langle f_{U(F)} \rangle$ and standard deviations $\sigma_{U(F)}$ obtained in experiments done at different [Mg^{2+}] and at loading rates of 1.8 pN/s (red) and 12.5 pN/s (blue). Full symbols refer to unfolding and empty symbols to folding. (**C**) Log-Linear plot of the transition rates versus force. Experiments were done at 0.00 mM [Mg^{2+}] for loading rates of 1.8 pN/s (dark red) and 12.5 pN/s (red), at 0.01 mM [Mg^{2+}] for loading rates of 1.8 pN/s (dark green) and 12.5 pN/s (green), at 0.1 mM [Mg^{2+}] for loading rates of 1.8 pN/s (dark blue) and 12.5 pN/s (blue), at 0.5 mM [Mg^{2+}] for loading rates of 1.8 pN/s (dark violet) and 12.5 pN/s (magenta), at 1 mM [Mg^{2+}] for loading rates of 1.8 pN/s (dark cyan) and 12.5 pN/s (cyan), at 4 mM [Mg^{2+}] for loading rates of 1.8 pN/s (dark orange) and 12.5 pN/s (orange), and at 10 mM [Mg^{2+}] for loading rates of 1.8 pN/s (gray) and 12.5 pN/s (black). (**D**) Dependence of the effective barrier $B_{\rm eff}(f)$ on force at different [Mg^{2+}]. Color code as in (**C**).

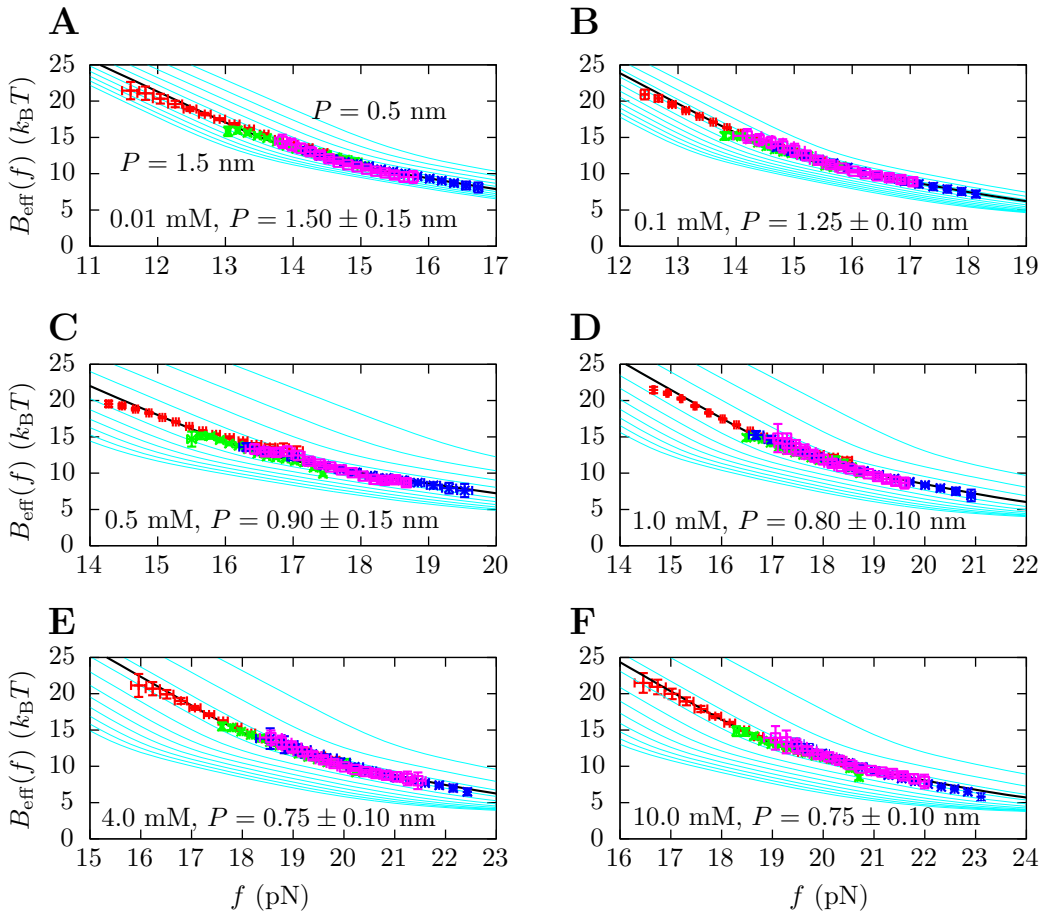

Figure 8. Determination of the persistence length of ssRNA at varying [Mg^{2+}]. Estimators of $B_{\rm eff}^{(U/F)}(f)$ obtained experimentally were compared with the expected $B_{\rm eff}^{KT}(f)$ profiles for different values of P (0.5, 0.6, 0.7, 0.8, 0.9, 1.0, 1.1, 1.2, 1.3, 1.4 and 1.5 nm from top to bottom) using eq. 7 and eqs. 10. Red (green) points are the experimental estimators $B_{\rm eff}^{(F)}(f)$ at a pulling rate of 12.5 (1.8) pN/s. Blue (magenta) points are the experimental estimators of $B_{\rm eff}^{(U)}(f)$ at a pulling rate of 12.5 (1.8) pN/s. Light blue lines are the $B_{\rm eff}^{KT}(f)$ profiles for values of m not matched, and black lines are the experimental estimators of $B_{\rm eff}(f)$ that match the experiments. Application of the method for experiments done at 0.01 mM [Mg^{2+}] (**A**), 0.1 mM [Mg^{2+}] (**B**), 0.5 mM [Mg^{2+}] (**C**), 1 mM [Mg^{2+}] (**D**), 4 mM [Mg^{2+}] (**E**), and 10 mM [Mg^{2+}] (**F**).

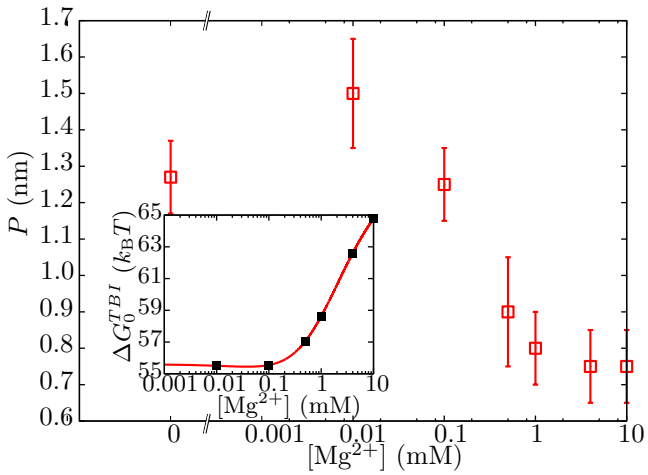

Figure 9. Dependence of the persistence length P on $[Mg^{2+}]$. Main panel: Experimental persistence length versus $[Mg^{2+}]$. Inset: Dependence of the free energy of formation of the RNA hairpin $\Delta G_{\mathrm{N}}^{\mathrm{TBI}}(0)$ on $[Mg^{2+}]$ with fixed 50 mM $[Mon^{+}]$ obtained using the TBI model [44, 45]. Black points are the values of the free energy of formation that we used for our analysis.

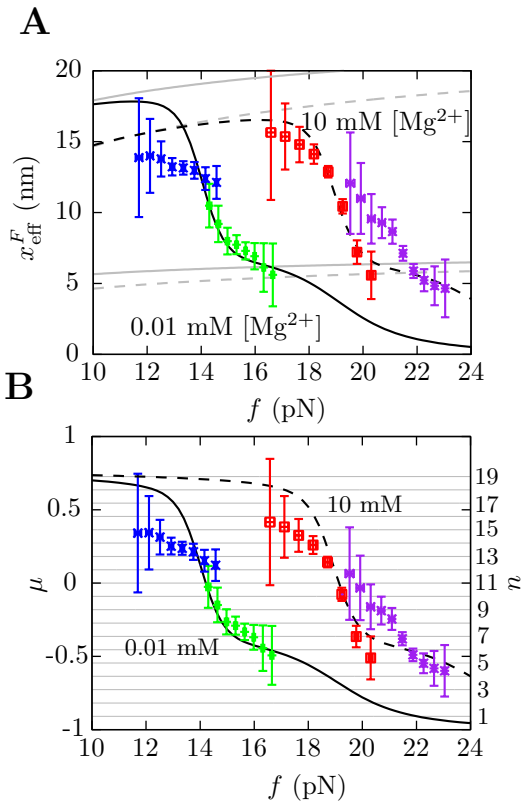

Figure 10. Barrier location and mechanical fragility at 0.01 mM and 10 mM [Mg^{2+}]. (**A**) Force-dependence of the barrier position measured with respect to the F state, $x_{\rm eff}^F(f)$. Continuous gray line is the WLC prediction of the molecular extension when $n = 19$ or $n = 6$ bps are unzipped at 0.01 mM [Mg^{2+}], and dashed gray line corresponds to the WLC prediction when $n = 19$ or $n = 6$ bps are unzipped at 10 mM [Mg^{2+}]. At an intermediate range of force the TS coincides with $n = 6$ for both ionic conditions. (**B**) Dependence of fragility $\mu(f)$ at 0.01 mM and 10 mM [Mg^{2+}]. Gray lines indicate the value of the fragility for different locations n of the TS along the stem. Continuous black lines are the theoretical prediction using Kramers rate theory for data at 0.01 mM [Mg^{2+}], and dashed black lines for data at 10 mM [Mg^{2+}]. Blue and green points are the experimental evaluation of $x_{\rm eff}^F(f)$ and $\mu(f)$ for folding and unfolding data collected at 0.01 mM [Mg^{2+}]. Red and purple points are the experimental evaluation for folding and unfolding at 10 mM [Mg^{2+}].

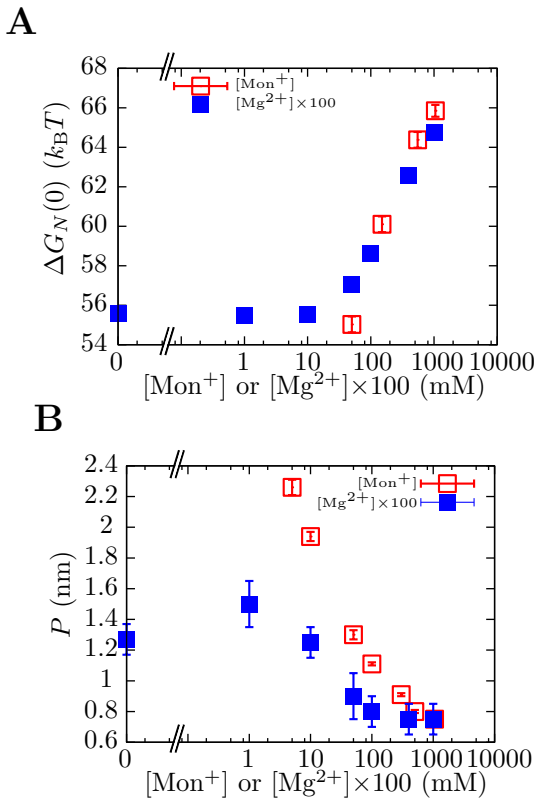

Figure 11. Comparison between [Mon$^+$] and [Mg^{2+}] results. (**A**) Free energy of formation of the RNA hairpin at different salt conditions. Magnesium concentrations have been multiplied by 100 along the horizontal axis. (**B**) Persistence length values for the ssRNA hairpin at different salt conditions. Magnesium concentrations have been multiplied by 100 along the horizontal axis.

8 Tables

[Mon^+] (mM)	P (nm)	$\log k_0$ (1/s)	$\Delta G_{\mathrm{N}}(0)$ ($k_{\mathrm{B}}T$)
1050	0.75±0.05	10.9±0.4	65.1±0.3
550	0.82±0.02	10.5±0.4	64.0±0.4
150	1.01±0.01	11.3±0.5	59.4±0.4
50	1.27±0.03	12.4±0.4	54.0±0.4

Table 1: **Parameters obtained from experiments at different [$\mathbf{Mon^+}$].** ssRNA persistence length P, $\log k_0$, and free energy of formation ($\Delta G_{\mathrm{N}}(0)$) for the RNA hairpin at different monovalent ion concentrations.

[Mg^{2+}] (mM)	P (nm)	$\log k_0$ (1/s)	$\Delta G_{\mathrm{N}}^{TBI}(0)$ ($k_{\mathrm{B}}T$)	g_2 (kcal/mol)
0.00	1.27±0.03	12.40±0.40	55.58	0.000±0.005
0.01	1.50±0.15	12.05±0.30	55.50	-0.007±0.005
0.10	1.25±0.10	11.45±0.30	55.55	-0.005±0.005
0.50	0.90±0.15	11.50±0.30	57.06	0.0393±0.005
1.00	0.80±0.10	11.40±0.50	58.63	0.0858±0.005
4.00	0.75±0.10	11.15±0.50	62.60	0.2033±0.005
10.0	0.75±0.10	10.40±0.50	64.77	0.2678±0.005

Table 2: **Parameters obtained for experiments at different [$\mathbf{Mg^{2+}}$].** Persistence length for ssRNA P, $\log k_0$, theoretical predictions for the free energies of formation based on the TBI model, $\Delta G_{\mathrm{N}}^{TBI}(0)$, and sequence-independent correction $g_2([Mg^{2+}])$ for the RNA hairpin at different magnesium concentrations. A fixed concentration of 50 mM [Mon^+] was used in all ionic conditions.

Supporting Material

9 Molecules studied

[Mon^+] (mM)	[Mg^{2+}] (mM)	loading rate (pN/s)	Molecules	Total cycles
50	0	1.8	4	95
50	0	12.5	2	376
150	0	1.8	6	292
150	0	12.5	4	329
550	0	1.8	5	163
550	0	12.5	3	501
1050	0	1.8	9	185
1050	0	12.5	9	405
50	0.01	1.8	5	146
50	0.01	12.5	5	386
50	0.1	1.8	7	374
50	0.1	12.5	9	1434
50	0.5	1.8	2	112
50	0.5	12.5	2	533
50	1.0	1.8	4	205
50	1.0	12.5	6	2183
50	4.0	1.8	7	385
50	4.0	12.5	7	1112
50	10.0	1.8	7	190
50	10.0	12.5	3	1189

Table 3: Number of molecules and total cycles measured at each ionic salt condition.

10 Study of fraying

The phenomenon of "fraying" at the ends of DNA and RNA duplexes can potentially interfere with both solution and single-molecule measurements of DNA and RNA stabilities, and it was previously suggested that its effects should be introduced in data analysis [55]. In order to check if fraying has an important role in our sequence, we computed the released (absorbed) molecular extension Δx_m in the unfolding (folding) process. This can be done using the expression:

$$\Delta x_m = \frac{\Delta f}{k_{\rm eff}} \tag{17}$$

where Δf is the force jump measured along the force-distance curve (FDC) and $k_{\rm eff}$ is its slope before the transition. The change in the molecular extension is also equal to:

$$\Delta x_m = x_N(f) - x_n(f) \tag{18}$$

where $x_N(f)$ is the equilibrium end-to-end distance of the unzipped hairpin evaluated at the unfolding/folding force ($N = 20$ in this case); $x_n(f)$ is the projection of the folded hairpin along the force axis; and n denotes the number of open/frayed base pairs in the F state. Ideally, in the absence of fraying, $n = 0$. However, in presence of fraying we should find the value $n > 0$ such that eq. (17) and (18) give the same change in molecular extension.

From the FDC we obtain $\Delta f = 1.2 \pm 0.1$ pN and $k_{\rm eff} = 0.0625 \pm 0.0146$ pN/nm which, using eq. (17), gives $\Delta x_m = 19 \pm 2$ nm for any salt concentration. On the other hand, we evaluate $x_N(f)$ and $x_{n=0}(f)$ using the elastic properties summarized in Tables 1 and 2 at the measured unfolding/folding forces. Using eq. (18) for $n = 0$ we obtain that predicted values for Δx_m lie in the range between 18.2 and 19.7 nm. Therefore, we conclude that fraying is not important for the molecule under study because the experimental evaluation of Δx_m (eq. (17)) is in agreement with the estimation of the released molecular extension for $N = 20$ and $n = 0$.

The effect of fraying has been proved to play an important role in former single-molecule stretching experiments, like in Woodside *et. al.* [55]. To understand when fraying is relevant in RNA or DNA hairpins we can take a look to sequences at the beginning of the stem as a higher GC-content makes the structure more stable. For instance, the RNA hairpin studied here starts with 5'-GCG-3', whereas most sequences studied by Woodside *et al.* [55] start with 5'-GAG-3' (except two sequences that start with 5'-TAT-3' and 5'-AAG-3'). In Table 4 we compute the free energy difference $\Delta G_1(f)$ at 1 M NaCl between the completely folded conformation ($n = 0$) and the frayed configuration with one open distal base pair ($n = 1$) at different values of force for our RNA hairpin and molecule 20R55/4T in [55]. At zero force, $\Delta G_1^{20R55/4T}(0)$ is below 3 $k_{\rm B}T$ and consequently thermal fluctuations can overcome the energetic barrier and the frayed conformation can take place. However, in the case of our hairpin ΔG_1 is too high for thermal fluctuations to overcome the energetic barrier. The same trend is observed at 10 pN. At 20 pN fraying is irrelevant because both molecules are in the unfolded state.

Force (pN)	$\Delta G_1^{20R55/4T}$ ($k_\mathrm{B}T$)	ΔG_1^{RNA} ($k_\mathrm{B}T$)
0	2.67	6.45
10	1.08	4.86
20	-1.34	2.45

Table 4: Free energy differences between frayed ($n = 1$) and completely closed structures ($n = 0$) of 20R55/4T hairpin [55] and our RNA hairpin at 1 M NaCl and different forces.

Motivated by solution measurements [94, 27], we also considered the possibility of fraying at the opposite end of the stem, on the base pairs closest to the loop. However, we found free energy differences of more than 10 $k_\mathrm{B}T$ between these configurations and the closed configuration, and consequently we conclude that these "frayed" configurations are not affecting our results.

Based on these considerations, we conclude that fraying plays a rather minor role (if any) on the thermodynamics and kinetics of folding/unfolding of the RNA hairpin and can be neglected.

11 Derivation of the effective barrier $\mathbf{B_{eff}^{KT}(f)}$

Here we derive the analytical expression for the effective barrier of a one-dimensional free energy landscape based on the work by Hyeon and Thirumalai [65].

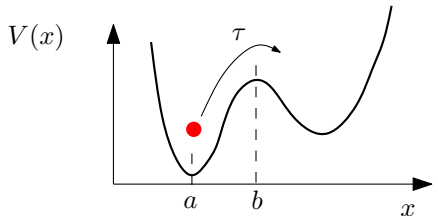

Figure 1: Brownian particle in a double well potential.

Suppose the system sketched in Fig. 1, where a Brownian particle is subject to the one dimensional potential $V(x)$. The time evolution of the probability density function (pdf) $p(x,t)$ to find the particle at the position x at time t follows the Fokker-Planck equation [65, 64]:

$$\begin{aligned}\frac{\partial p(x,t)}{\partial t} &= D\frac{\partial}{\partial x}\left[\frac{\partial}{\partial x}+\frac{1}{k_\mathrm{B}T}\frac{dV(x)}{dx}\right]p(x,t)\\ &= D\frac{\partial}{\partial x}\left[e^{-\frac{V(x)}{k_\mathrm{B}T}}\frac{\partial}{\partial x}e^{\frac{V(x)}{k_\mathrm{B}T}}\right]p(x,t)\\ &= \mathcal{L}_\mathrm{FP}\left[p(x,t)\right]\end{aligned} \tag{19}$$

Where D is the diffusion coefficient and $\mathcal{L}_{FP}$ is the Fokker-Plank operator. If we suppose that the particle initially is located at $x = a$, $p(x,0) = \delta(x-a)$, the formal solution of equation

(19) is:

$$p(x,t) = e^{t\mathcal{L}_{FP}}\delta(x-a) \tag{20}$$

We want to evaluate the average time τ it takes to the Brownian particle to jump the kinetic barrier located at $x = b$. In order to simplify the following calculations, we suppose that there are absorbing conditions at $x = b$: once the particle reaches the maximum sketched in Fig. 1 it always goes to the right well. The probability to find the particle in the left well of the potential $V(x)$ ($x \in [-\infty, b]$) at time t, also known as the survival probability $S(t)$, can be defined as:

$$S(t) = \int_{-\infty}^{b} dx\ p(x,t) \tag{21}$$

The time derivative of the survival probability is equal to the time survival pdf $\rho(t)$, that is, the pdf of the time it takes to the Brownian particle to cross the barrier located at $x = b$.

$$S(t+dt) - S(t) = -\rho(t)dt \Rightarrow \rho(t) = -\frac{\partial S(t)}{\partial t} \tag{22}$$

Therefore, the mean first passage time τ can be calculated as:

$$\begin{aligned}
\tau &= \int_0^\infty dt\ t\ \rho(b,t) \\
&= \int_0^\infty dt\ S(b,t) \\
&= \int_0^\infty dt \int_{-\infty}^{b} dx\ p(x,t) \\
&= \int_0^\infty dt \int_{-\infty}^{b} dx\ e^{t\mathcal{L}_{FP}}\delta(x-a) \\
&= \int_0^\infty dt \int_{-\infty}^{b} dx\ \delta(x-a)e^{t\mathcal{L}^\dagger_{FP}}1 \\
&= \int_0^\infty dt\ e^{t\mathcal{L}^\dagger_{FP}}1
\end{aligned} \tag{23}$$

In order to obtain this expression we integrated by parts and used that the adjoint operator satisfies $f(x)\mathcal{L}\left[g(x)\right] = g(x)\mathcal{L}^\dagger\left[f(x)\right]$. If we apply the adjoint Fokker-Plank operator $\mathcal{L}^\dagger_{FP}$ at both sides of equation (23) we obtain:

$$\begin{aligned}\mathcal{L}_{FP}^{\dagger}\tau &= \int_0^{\infty} dt\ \mathcal{L}_{FP}^{\dagger} e^{t\mathcal{L}_{FP}^{\dagger}} 1 \\ &= \int_0^{\infty} dt\ \frac{de^{t\mathcal{L}_{FP}^{\dagger}}}{dt} 1 \\ &= -1 \end{aligned} \tag{24}$$

Which gives a differential equation for the survival time τ that depends on the adjoint Fokker-Plank operator.

It can be demonstrated that:

$$\mathcal{L}_{FP}^{\dagger} = De^{\frac{V(x)}{k_{\mathrm{B}}T}} \frac{\partial e^{-\frac{V(x)}{k_{\mathrm{B}}T}}}{\partial x} \frac{\partial}{\partial x} \tag{25}$$

and we can write the following differential equation:

$$\mathcal{L}_{FP}^{\dagger}\tau(x) = De^{\frac{V(x)}{k_{\mathrm{B}}T}} \frac{\partial}{\partial x}\left(e^{-\frac{V(x)}{k_{\mathrm{B}}T}}\right) \frac{\partial}{\partial x}\tau(x) = -1 \tag{26}$$

In order to solve eq. (26) we use the absorbing boundary condition $\tau(b) = 0$ and the reflecting boundary $\frac{\partial \tau}{\partial x}|_{x=a} = 0$.

$$\tau(x) = \frac{1}{D}\int_x^b dy\ e^{\frac{V(y)}{k_{\mathrm{B}}T}} \int_a^y dx e^{-\frac{V(x)}{k_{\mathrm{B}}T}} \tag{27}$$

Once we have evaluated the average survival time of the Brownian particle, we want to evaluate the effective barrier of the potential $V(x)$. Using the phenomenological Arrhenius approach [95] that considers that the survival time depends on the exponential of the barrier we can write:

$$\tau \simeq e^{\frac{B_{\mathrm{eff}}}{k_{\mathrm{B}}T}} \Rightarrow B_{\mathrm{eff}} = k_{\mathrm{B}}T\log\left(\tau/\tau_0\right) \tag{28}$$

$$B_{\mathrm{eff}} = k_{\mathrm{B}}T\log\left(\frac{1}{\tau_0 D}\int_x^b dy\ e^{\frac{V(y)}{k_{\mathrm{B}}T}} \int_a^y dx e^{-\frac{V(x)}{k_{\mathrm{B}}T}}\right) \tag{29}$$

τ_0 is related to the diffusion time of the particle the along x axis. By discretization of equation (29) we obtain the expression (7) of the main paper,

$$B_{\mathrm{eff}}(f) = k_{\mathrm{B}}T\log\left[\sum_{n=0}^{N} e^{\frac{\Delta G_{\mathrm{n}}(f)}{k_{\mathrm{B}}T}} \left(\sum_{n'=0}^{n} e^{-\frac{\Delta G_{\mathrm{n}'}(f)}{k_{\mathrm{B}}T}}\right)\right] \tag{30}$$

Where ΔG_n is the potential energy $V(x)$ and where we considered that $D\tau_0 \simeq \mathcal{O}(1)$.

12 Sensitivity of the data analysis

An experimental estimation of the kinetic barrier is obtained from the measured transition rates $k_U(f)$ and $k_F(f)$. From the unfolding transition rate, the estimator of the kinetic barrier is given by:

$$\frac{B_{\rm eff}^{(U)}(f)}{k_{\rm B}T} = \log k_0 - \log k_U(f) \tag{31}$$

Where $\log k_0$ is a constant (equal to the logarithm of the attempt rate at zero force for the activated kinetics) and $\log k_U(f)$ is estimated from the measured unfolding rupture forces (see section 2.6 in the main paper).

On the other hand, from folding rupture forces the estimation of the kinetic barrier is:

$$\begin{aligned}\frac{B_{\rm eff}^{(F)}(f)}{k_{\rm B}T} &= \log k_0 - \log k_F(f) + \frac{\Delta G_{\rm N}(f)}{k_{\rm B}T} \\ &= \log k_0 - \log k_F(f) + \frac{\Delta G_{\rm N}(0)}{k_{\rm B}T} + \frac{\Delta G_{\rm N}^{ssRNA}(f)}{k_{\rm B}T} + \frac{\Delta G_{\rm N}^{d_0}(f)}{k_{\rm B}T} \\ &= \log k_0 - \log k_F(f) + \frac{\Delta G_{\rm N}(0)}{k_{\rm B}T} - \frac{\int_0^f x_{\rm N}^{ssRNA}(f')df'}{k_{\rm B}T} + \log\left[\frac{k_{\rm B}T}{fd_0}\sinh\left(\frac{fd_0}{k_{\rm B}T}\right)\right]\end{aligned} \tag{32}$$

Where $\log k_0$ is the same constant as in eq. (31) and $\log k_F(f)$ is obtained from the measured folding rupture forces. The term $\Delta G_{\rm N}(0)/k_{\rm B}T$ is another constant equal to the free energy of the RNA hairpin at zero force; $\int_0^f x_{\rm N}^{ssRNA}(f')df'$ is a force dependent term evaluated according to the model used to describe the elastic response of ssRNA (here we use the WLC model with a salt-dependent persistence length P); and the last term, $\log\left[\frac{k_{\rm B}T}{fd_0}\sinh\left(\frac{fd_0}{k_{\rm B}T}\right)\right]$, is evaluated using $d_0 = 2.0$ nm at any salt condition for the given force f (see section 2.3).

Typically, $\log k_0$ is unknown and either $\Delta G_N(0)/k_{\rm B}T$ is unknown and P is known (here, for monovalent salt conditions) or $\Delta G_N(0)/k_{\rm B}T$ is known and P is unknown (for mixed monovalent/Mg^{2+} conditions).

12.1 Sensitivity of the method at determining $\Delta \mathbf{G_N}(\mathbf{0})$

For a given value of the persistence length P we can evaluate the kinetic barrier from experimental unfolding/folding rupture forces by ignoring the unknown constants ($\log k_0$ and $\Delta G_N(0)/k_{\rm B}T$) and we obtain the result shown in Fig. 2A. Error bars are evaluated using the bootstrap method.

In order to determine the constant $\Delta G_N(0)/k_{\rm B}T$, *i. e.* the free energy of formation of the RNA hairpin, we impose the continuity of the kinetic barrier in folding and unfolding data (Fig. 2B). The error committed in the evaluation of $\Delta G_N(0)/k_{\rm B}T$ mainly depends on the good agreement of the overlapping between $\left(B_{\rm eff}^{(U)}(f) - \log k_0\right)$ and $\left(B_{\rm eff}^{(F)}(f) - \log k_0\right)$ and their error bars. In the example provided in Fig. 2B the best overlapping is found at $\Delta G_N(0) = 64\ k_{\rm B}T$. In the insets we see that the continuity requirement worsens for values of $\Delta G_N(0)$ as close as

64.4 or 63.6 k_BT. As a consequence, we estimate $\Delta G_N(0) = 64.0 \pm 0.4\ k_BT$ (see Table 1 in the main document).

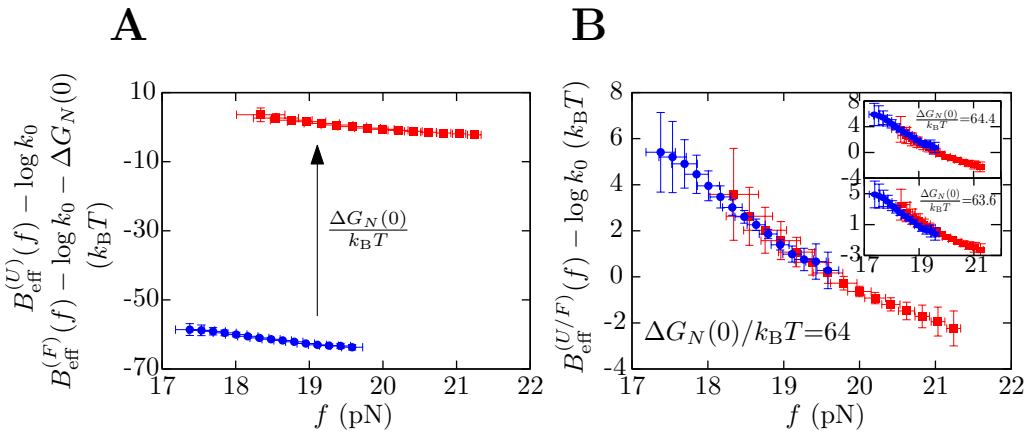

Figure 2: **Determination of $\Delta G_N(0)$.** Data obtained at 1.8 pN/s and 550 mM [Mon^+]. **(A)** Evaluation of $B^{(U)}(f) - \log k_0$ (red squares) and $B^{(F)}(f) - \log k_0 - \Delta G_N(0)/k_BT$ (blue circles). **(B)** $\Delta G_N(0)/k_BT$ is obtained using the overlapping of the kinetic barrier with force. Once unfolding and folding data overlap, the resulting experimental curve is equal to $B_{\rm eff}(f) - \log k_0$. *Insets*: The value of $\Delta G_N(0)/k_BT$ can be overestimated (top) or underestimated (bottom) so that the continuity requirement is not well-satisfied.

12.2 Sensitivity of the method at determining $\log k_0$

In order to estimate the attempt rate at zero force we need a theoretical model for the kinetic barrier. In the case of this work we use the Kramers theory (see section 11). Once we have evaluated $B_{\rm eff}(f) - \log k_0$, $\log k_0$ is obtained by overlapping the theoretical model to the experimental results, as shown in Fig. 3. The sensitivity in the determination of $\log k_0$ is similar to the sensitivity in determining $\Delta G_N(0)$: at $\log k_0$=10.5 we find the best match, and for values 0.4 greater or smaller the result significantly worsens (insets in Fig. 3B).

12.3 Sensitivity of the method at determining P

The elastic contribution to $B_{\rm eff}(f)$ only applies to folding data, eq. (32), and regulates the slope of the experimental estimation of the kinetic barrier in the range of experimentally measured folding forces. In this work we determine the persistence length P of ssRNA by comparing the profile of the kinetic barrier estimated from experimental data with the one evaluated using the Kramers theory (see Fig. 4). The sensitivity at determining P is limited by the determination of $\Delta G_N(0)/k_BT$, $\log k_0$ and the error bars estimated for $B^{(U/F)}_{\rm eff}(f)$. Therefore, the is a feedback in the determination of the $\Delta G_N(0)/k_BT$, $\log k_0$ and P: optimal values are those that give a best fit between experimental and theoretical estimations of the kinetic barrier.

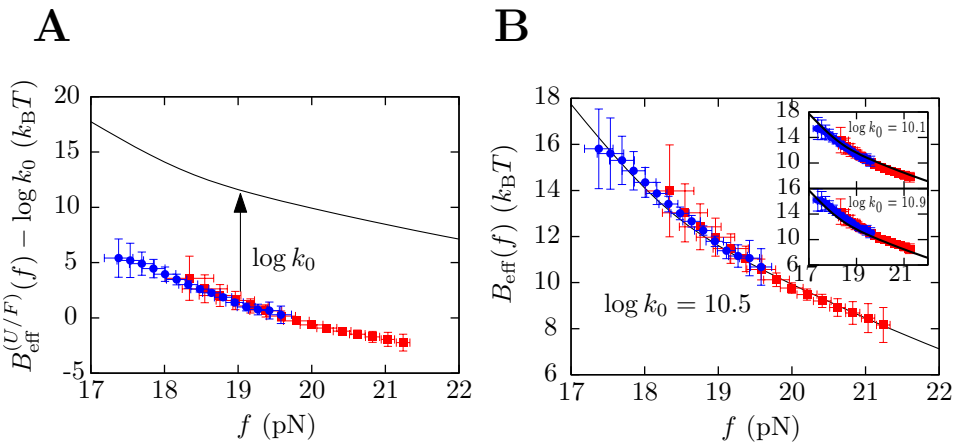

Figure 3: **Determination of $\log k_0$.** Data obtained at 1.8 pN/s and 550 mM [Mon^+]. **(A)** Black-straight line is the theoretical evaluation of the kinetic barrier using Kramers theory (section S3 and section 2.5 in the main document) and blue circles (red squares) are the experimental estimation of the kinetic barrier without the contribution of $\log k_0$ using folding (unfolding) rupture forces. **(B)** $\log k_0$ is obtained overlapping the experimental data to the theoretical curve. *Insets*: The value of $\log k_0$ can be underestimated (top) or overestimated (bottom) leading to a worse match between theory and experiments.

The same methodology was used to determine the value of m in the non-specific correction for the free energy of formation of one base pair, where the elastic parameters are known but the free energy is unknown (see section 3.5 and Fig. 4 in the main paper): we look for the best matching between theory and experiments.

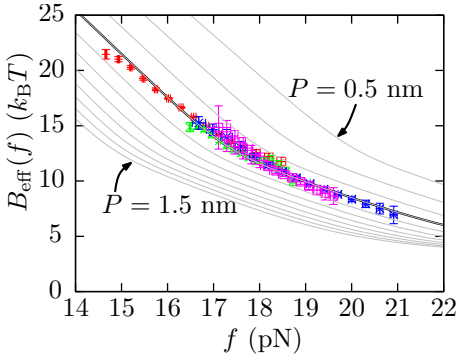

Figure 4: **Determination of P.** Data obtained at 1 mM [Mg^{2+}]. Gray lines are evaluations of the kinetic barrier using Kramers theory, eq. (30), for different values of the persistence length ($P = 0.5, 0.6, 0.7, \ldots, 1.5$ nm). Experimental data is analyzed using also different values of the persistence length. In this case, at $P = 0.8 \pm 0.1$ nm we obtain the best overlapping between theory and experiments.

13 UV Absorbance experiments

In order to determine the effect of salt on the stability of the hairpin we obtained the melting profile of the molecule using UV absorbance at 260 nm. The melting temperature was measured at 70±1°C using a buffer containing 100 mM Tris.HCl, 1 mM EDTA and no NaCl neither $MgCl_2$. Results can be observed in Fig. 5A. We calculated the first derivative of the absorbance as a function of temperature (Fig. 5B) and observed several maximums along the resulting profile (see arrows), which denote the presence of pre-melted states. For instance, regions with a richer A-U content in the middle of the stem may dissociate before the whole hairpin is unfolded (Fig. 5C). This result invalidates the two-states assumption used to extract thermodynamic parameters from the melting curve.

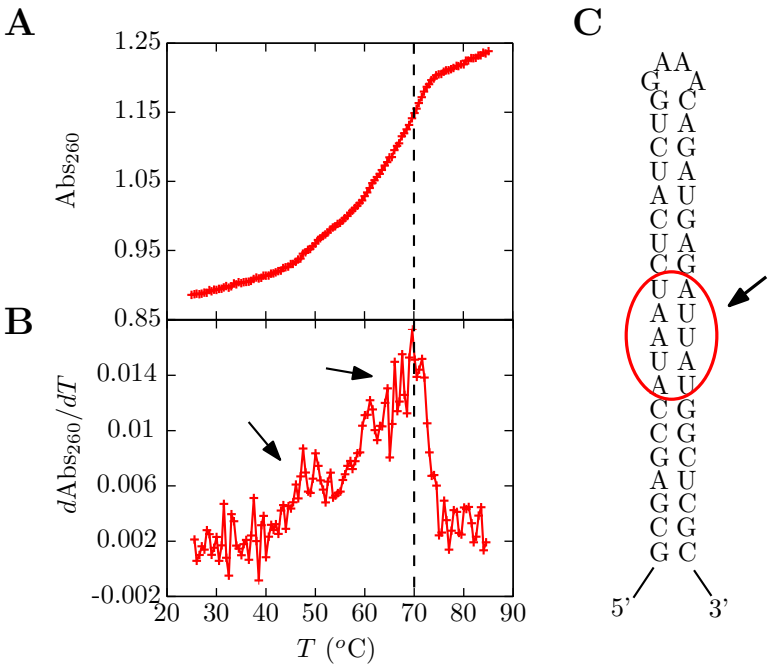

Figure 5: UV Absorbance of the RNA hairpin. **(A)** Experimental results of the absorbance of our RNA hairpin as a function of temperature. **(B)** First derivative of the absorbance as a function of temperature. Its maximum (black dashed line) defines the melting temperature. **(C)** The RNA hairpin under study has a region with a high A-U content in the stem which could lead to premelted states.

We tried to obtain the melting profile adding 100 mM NaCl to the buffer, and the melting temperature was too high and the sample started boiling and evaporating before any relevant signal could be obtained. Therefore, for this RNA hairpin melting curves cannot be measured at the experimental conditions used in our pulling experiments with optical tweezers, and our results can only be compared with Mfold [15, 19, 68] and other theoretical predictions [81, 96, 86]

14 Rupture force histograms

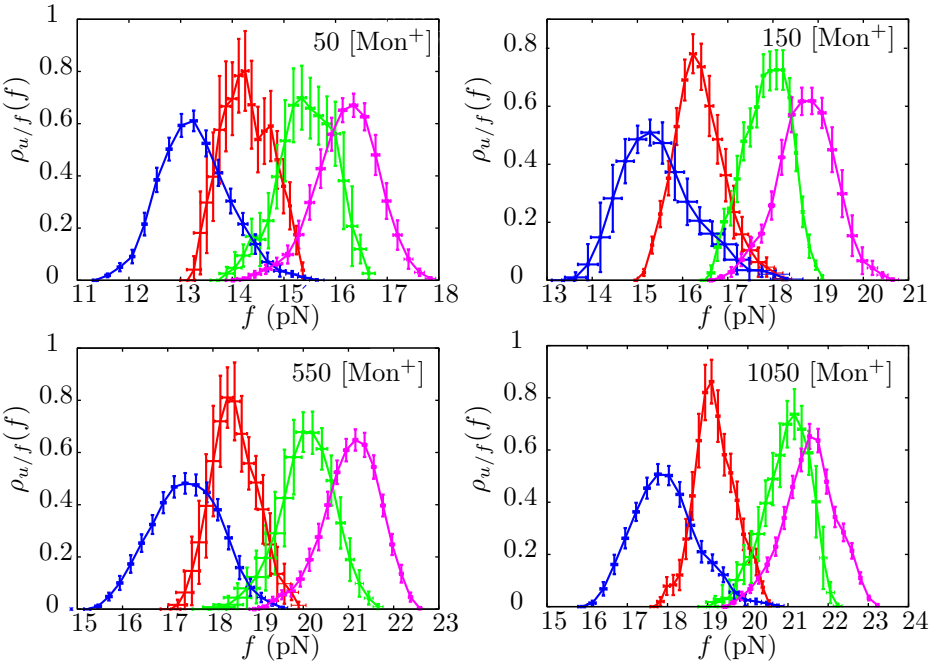

Figure 6: Probability distributions of the unfolding and folding first rupture forces measured at different pulling speeds and different monovalent ionic condition. Red points are folding forces at 1.8 pN/s, green are unfolding forces at 1.8 pN/s, blue are folding forces at 12.5 pN/s and magenta are unfolding forces at 12.5 pN/s.

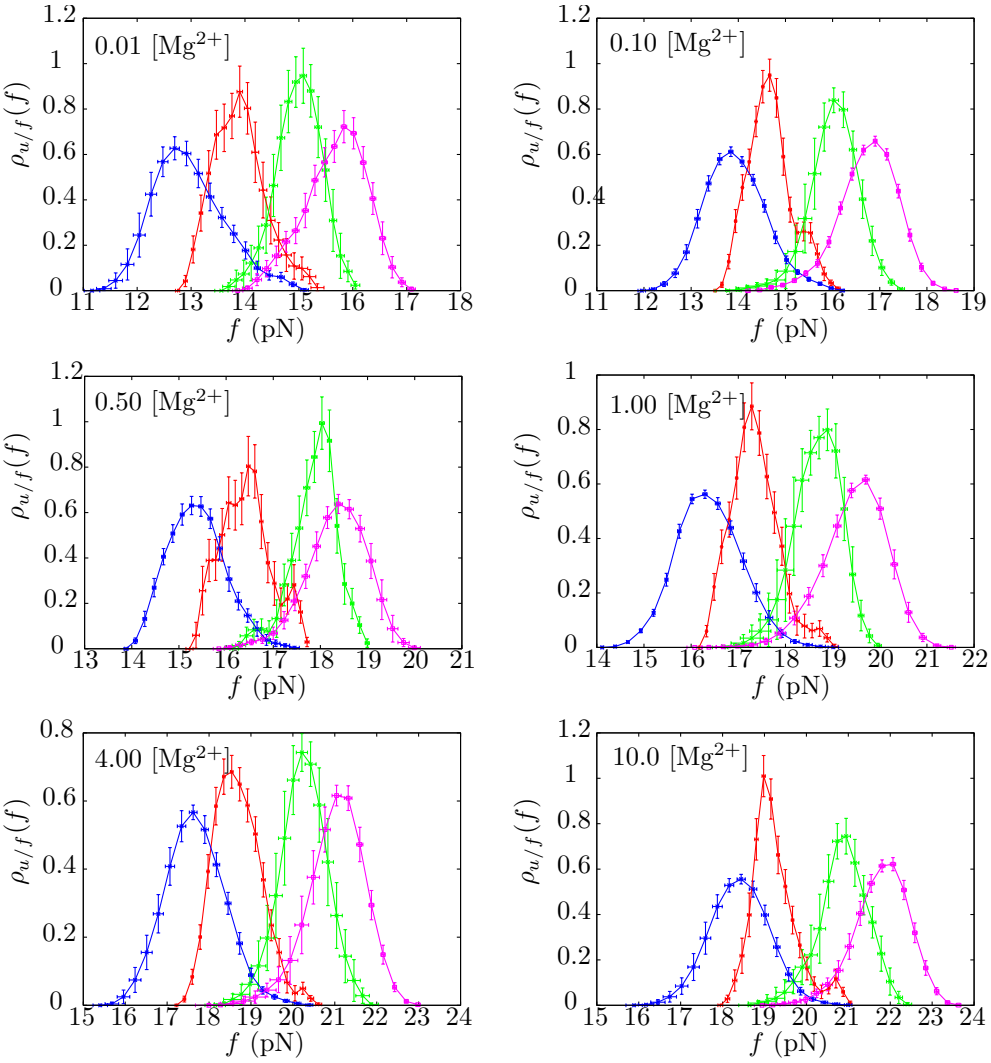

Figure 7: Probability distributions of the first rupture forces measured at different pulling speeds and different magnesium concentration. Red points are folding forces at 1.8 pN/s, green are unfolding forces at 1.8 pN/s, blue are folding forces at 12.5 pN/s and magenta are unfolding forces at 12.5 pN/s.

15 Tightly Bound Ion Model

In this section the empirical equations of the Tightly Bound Ion (TBI, [96, 86]) model used to predict the hairpin free energies at different ionic conditions are summarized [44, 45].

The external parameters, obtained from the Mfold server [15, 19, 68], are:

Bases in the loop	N_l=4
Bases in the helix	N=20
Hairpin diameter	d=1.7 nm
Interphosphate distance	a=0.6 nm
Enthalpy at 1 M [Mon^+], 0 M [Mg^{2+}]	ΔH_0=199 kcal/mol
Entropy at 1 M [Mon^+], 0 M [Mg^{2+}]	ΔS_0=527.16 mkcal/Kmol

In what follows x is the concentration of monovalent salt and y is the concentration of magnesium ions. Both parameters are given in units of M. Temperature T is given in Celsius.

The empirical set of equations are:

$$\ln Z^l_{Mon}(x) = a^l_1(x)\log(N_l - a/d + 1) + b^l_1(x)(N_l - a/d + 1)^2 - b^l_1(x) \tag{33}$$

$$\ln Z^c_{Mon}(x) = c^l_1(x)N_l - d^l_1(x) \tag{34}$$

$$a^l_1(x) = (0.02N_l - 0.026)\log(x) + 0.54N_l + 0.78 \tag{35}$$

$$b^l_1(x) = \left(-\frac{0.01}{(N_l+1)} + 0.006\right)\log(x) - \frac{7}{(N_l+1)^2} - 0.01 \tag{36}$$

$$c^l_1(x) = 0.07\log(x) + 1.8 \tag{37}$$

$$d^l_1(x) = 0.21\log(x) + 1.5 \tag{38}$$

$$G^l_{Mon}(x) = -(\ln Z^l_{Mon}(x) - \ln Z^c_{Mon}(x)) \tag{39}$$

$$G^h_{Mon}(x,T) = H_0 - (T + 273.15)S_{Mon}(x)0.001 \tag{40}$$

$$S_{Mon}(x) = S_0 - 3.22(N-1)g_1(x) \tag{41}$$

$$g_1(x) = a^h_1(x) + b^h_1(x)/N \tag{42}$$

$$a^h_1(x) = -0.075\log(x) + 0.012\log^2(x) \tag{43}$$

$$b^h_1(x) = 0.018\log^2(x) \tag{44}$$

$$G_{Mon}(x,T) = G^h_{Mon}(x,T) + G^l_{Mon}(x) \tag{45}$$

$$\ln Z^l_{Mg}(y) = a^l_2(y)\log(N_l - a/d + 1) + b^l_2(y)(N_l - a/d + 1)^2 - b^l_2(y) \tag{46}$$

$$\ln Z^c_{Mg}(y) = c^l_2(y)N_l - d^l_2(y) \tag{47}$$

$$a^l_2(y) = \left(-\frac{1}{N_l + 1} + 0.32\right)\log(y) + 0.7N_l + 0.43 \tag{48}$$

$$b^l_2(y) = 0.0002(N_l + 1)\log(y) - 5.9/(N_l + 1)^2 - 0.003 \tag{49}$$

$$c^l_2(y) = 0.067\log(y) + 2.2 \tag{50}$$

$$d^l_2(y) = 0.163\log(y) + 2.53 \tag{51}$$

$$G^l_{Mg}(y) = -(\ln Z^l_{Mg}(y) - \ln Z^c_{Mg}(y)) \tag{52}$$

$$\tag{53}$$

$$G^h_{Mg}(y,T) = H_0 - (T + 273.15)S_{Mg}(y)0.001 \tag{54}$$

$$S_{Mg}(y) = S_0 - 3.22(N - 1)g_2(y) \tag{55}$$

$$g_2(y) = a^h_2(y) + b^h_2(y)/N^2 \tag{56}$$

$$a^h_2(y) = -0.6/N + 0.025\log(y) + 0.0068\log^2(y) \tag{57}$$

$$b^h_2(y) = \log(y) + 0.38\log^2(y) \tag{58}$$

$$G_{Mg}(y,T) = G^h_{Mg}(y,T) + G^l_{Mg}(y) \tag{59}$$

$$x^l_1(x,y) = x/(x + (7.2 - 20/N_l)(40 - \log(x))y) \tag{60}$$

$$G^l_{Mon,Mg}(x,y) = x^l_1(x,y)G^l_{Mon}(x) + (1 - x^l_1(x,y))G^l_{Mg}(y) \tag{61}$$

$$G^h_{Mon,Mg}(x,y,T) = H_0 - (T + 273.15)S_{Mon,Mg}(x,y)0.001 \tag{62}$$

$$S_{Mon,Mg}(x,y) = S_0 - 3.22\left[(N - 1)\left(x^h_1(x,y)g_1(x) + (1 - x^h_1(x,y))g_2(y)\right) + g_{1,2}(x,y)\right] \tag{63}$$

$$x^h_1(x,y) = \frac{x}{x + (8.1 - 32.4/N)(5.2 - \log(x))y} \tag{64}$$

$$g_{1,2}(x,y) = -0.6x^h_1(x,y)(1 - x^h_1(x,y))\log(x)\log((1/x^h_1(x,y) - 1)x)/N \tag{65}$$

$$\boxed{G_{Mon,Mg}(x,y,T) = G^h_{Mon,Mg}(x,y,T) + G^l_{Mon,Mg}(x,y)} \tag{66}$$

Where $G_{Mon,Mg}(x,y,T)$ is the free energy at any temperature and at any monovalent and magnesium ion concentration.

16 Comparison to the counterion condensation theory

There are two successful theories to account for the energetic interactions between ions in solution and nucleic acids: the Poisson-Boltzmann theory and the counterion condensation theory derived by Manning [81, 87]. These theories are based on different mean field approaches and neglect any kind of correlations between the ions in the solution. More recently a new theory known as the Tightly Bound Ion (TBI) model has been introduced [96], which accounts for the different modes of correlations between counterions.

In Fig. 8 we see the prediction provided by the Manning theory and the TBI model to the free energy of formation of our RNA hairpin as a function of the salt concentration. Because correlations between monovalent ions are negligible, we see that both the Manning theory and the TBI model give similar results under this condition (Fig. 8A). However, correlations between Mg^{2+} are important and the TBI model gives an improved prediction in this case (Fig. 8B) [86].

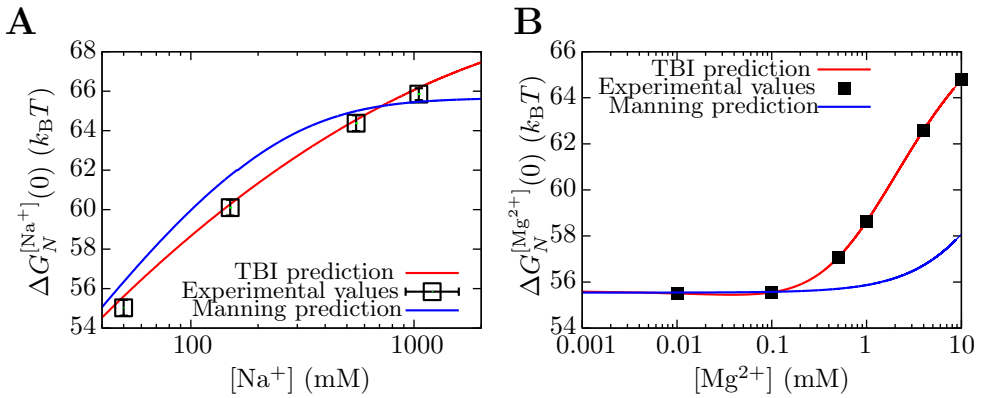

Figure 8: Comparison between experimental data, the counterion condensation theory and the TBI model to predict the behavior of the free energy of formation of our RNA hairpin as a function of salt concentration.